EXPERIMENTAL STUDY OF CONVECTION OF A BINARY FLUID IN A QUASI-1-DIMENSIONAL CELL

MINGHUI LIU, B.Sc.

Experimental Study of Convection of a Binary Fluid in a Quasi-1-dimensional Cell

by

© Minghui Liu, B.Sc.

A thesis submitted to the School of Graduate
Studies in partial fulfillment of the
requirements for the degree of
Master of Science

Department of Physics
Memorial University of Newfoundland

May 1992

St. John's Newfoundland

ISBN 0-315-73335-7

Canada

Abstract

Rayleigh-Bénard convection in binary fluids has been studied widely in recent years due to the richness of instability phenomena observed. With properly chosen parameters, the first bifurcation from conduction to convection can be to a traveling wave (TW) state, and there is then a second transition from the TW state to a stationary overturning convection (SOC) state. In this thesis, we report on an experimental study of TW and SOC states in ethanol-water mixtures in a narrow rectangular cell. The flow is visualized using the shadowgraph technique. By comparing our recorded shadowgraph intensity profiles with recent numerical results [13], we studied the temperature and concentration fields in the convective flow, both in the TW and SOC states. While our results confirm some of the qualitative features of the numerical results, there appear to be some significant differences which may be due partly to the narrow geometry of the experimental cell.

Acknowledgements

I wish to express my sincere appreciation to my supervisor Dr. John de Bruyn for his supervision throughout this project and for his help in preparing this thesis. I am grateful to Mr. W. Barten and Dr. M. Lücke for kindly providing us with their numerical results. I would also like to thank Mr. K.D. Eaton for useful discussions. My thanks are also given to the School of Graduate Studies of the Memorial University of Newfoundland for providing me a University Fellowship, to the Department of Physics and Dr. de Bruyn for providing me with teaching and research assistantships. This thesis is dedicated to my parents, who have always given me support and encouragement.

Contents

Abstract ii

Acknowledgements iii

List of Figures v

List of Tables vii

1 Introduction 1

2 Theory 13

2.1 Linear stability analysis for a pure fluid 14

2.1.1 Governing equations 14

2.1.2 Stability criteria 18

2.2 Binary fluids 19

2.2.1 The Soret effect 20

2.2.2 Governing equations 21

2.2.3 Stability criteria 24

2.3 Nonlinear theory 27

2.4 Some numerical results for ethanol-water mixtures 30

3 Experimental Apparatus and Procedure 37

3.1 Convection cell 38

3.2 Temperature control 40

3.3 Shadowgraph flow visualization 42

3.4 General procedure 45

4 Experimental Results and Analysis 48

4.1 Bifurcation properties 49

4.2 Structure of TW and SOC states 52

5 Conclusions 77

Bibliography 80

Appendix A: Some Properties of the Ethanol-water Mixture 84

List of Figures

1.1 Imbalance of forces is needed to initiate a convective flow. . . 3

1.2 Convection roll patterns in the Rayleigh-Bénard configuration. 5

1.3 Numerically calculated Nusselt numbers as a function of Rayleigh number for TW and SOC states. 10

2.1 Critical Rayleigh number vs. separation ratio for binary fluid mixtures with free-pervious boundary conditions 26

2.2 Convection amplitude as a function of Rayleigh number. . . . 29

2.3 Phase velocity of traveling waves as a function of Rayleigh number. 29

2.4 Isoconcentration lines for various unstable solutions. 31

2.5 Isoconcentration lines for various stable solutions. 31

2.6 Bifurcation properties of nonlinear convective states. 33

2.7 Phase diagram of $r-1$ vs. ψ for ethanol-water mixtures. . . . 34

2.8 Structural properties of TW and SOC convective states. . . . 35

3.1 Sketch of the convection cell. 39

3.2 Temperature control system 41

3.3 Shadowgraph system with parallel light through the convection cell. 43

3.1 Principle of the shadowgraph method: The incoming parallel light is deflected by the gradient of the refractive index. 44

4.1 Nusselt number $N-1$ as a function of Rayleigh number r. . . 58

4.2 Typical shadowgraph images. 59

4.3 Shadowgraph "space-time" images at various Rayleigh numbers, illustrating traveling wave convection over a range of r. . 61

4.4 Traveling wave frequency ω as a function of Rayleigh number. 62

4.5 Numerically calculated, vertically averaged temperature field, concentration field, their second derivatives and the optical profile. 63

4.6 Numerically calculated shadowgraph intensities at various vertical positions z of the cell. 66

4.7 The experimental shadowgraph intensity, averaged over z, for (a) a SOC state of the mixture at $r = 1.54$ and (b) convection in pure water at $r = 1.19$. 70

4.8 The experimental shadowgraph intensity, averaged over z, at various Rayleigh numbers. 72

4.9 The experimental shadowgraph intensity for a TW state with $r = 1.29$ at various z positions. 74

4.10 The experimental shadowgraph intensity profiles for TWs at various Rayleigh numbers, measured at a fixed point within the cell while the TWs passed by it. 76

List of Tables

A.1 Heat capacity for ethanol-water mixtures at various concentrations and temperatures. 85

A.2 Thermal conductivity λ for ethanol-water mixtures at various concentrations and temperatures. 85

A.3 Density ρ for ethanol-water mixtures at various concentrations and temperatures. 86

A.4 Viscosity μ for ethanol-water mixtures at various concentrations and temperatures. 87

Chapter 1

Introduction

Rayleigh-Bénard convection is one of the most extensively studied hydrodynamic systems and has been the subject of a tremendous amount of experimental and theoretical work. This interest is due in part to the fact that it is a nice, simple, well characterized system for the study of nonlinear dynamics, and also to the role played by convection in phenomena such as continental drift, solar granulation and the unpredictability of the weather.

The study of thermal convection can be traced back to the early 1900s, when the first systematic experimental investigations were undertaken by Bénard [1]. The convective system he studied was more complicated than he realized, and its true nature was not revealed until the 1960s. In an attempt to explain Bénard's results, Lord Rayleigh published a theoretical article on convection, based on linear stability analysis, in 1916 [2]. It is now known that Lord Rayleigh's theory does not apply to the system examined by Bénard; nevertheless, Lord Rayleigh's work is the starting point for almost all modern theories of convection.

Lord Rayleigh's theory can be explained in the context of a model experiment that employs a fluid with somewhat simpler properties than any real gas and liquid. A thin layer of the fluid is confined between two flat, rigid, horizontal plates and completely fills the space between them, so that there is no free surface. The layer is thin in that its horizontal extent is much greater than its depth, which is equal to the separation between the plates. This constraint is intended to remove the influence of the boundaries at the edges of the plates, which do not explicitly enter into the theoretical description. Ideally the layer would be of infinite horizontal extent; in practice the layer is always confined within a finite geometry, but a large aspect ratio of the horizontal size to the vertical size approximates this constraint. This experimental setup is often called the Rayleigh-Bénard configuration and has been used widely.

The fluid layer is heated from below, with the temperature of the top plate kept constant by a thermal sink. Thus, with a fixed amount of heat supplied to the bottom plate, the temperature of the bottom plate as well as the temperature difference are constant. Furthermore, in the absence of flow, the temperature gradient in the fluid is linear.

Consider a small parcel of fluid near the bottom of the layer, as shown in Figure 1.1. Because of the elevated temperature at the layer bottom, the parcel has a density that is less than the average density of the entire layer. As long as the parcel remains in place, however, it is surrounded by fluid of the same density, and so it has neutral buoyancy. All forces acting on it are in balance, and it neither rises nor sinks. Suppose now that through some random perturbations, the parcel of fluid is given a slight upward motion. The parcel is then surrounded by cooler, more dense fluid. As a result it has positive buoyancy, so that it tends to rise farther. However, the buoyancy

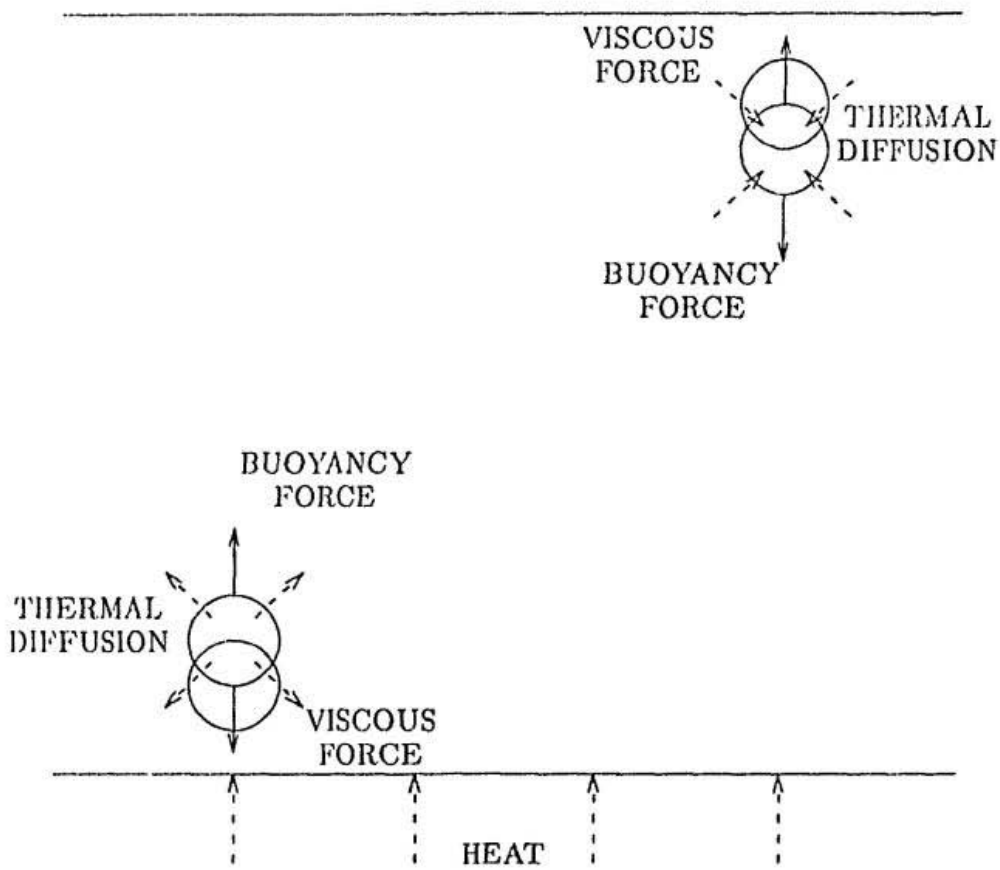

Figure 1.1: Imbalance of forces is needed to initiate a convective flow. For a thin layer of fluid between two rigid plates and heated from below,convection begins when buoyancy overcomes the dissipative effects of viscous drag and heat diffusion, or in other words when the Rayleigh number exceeds a critical value.

force is opposed by viscous drag and by the effect of heat diffusion, which tends to equalize the temperature of a displaced parcel and its environment, so the mere existence of a temperature gradient is not enough to ensure the onset of convective flow. It is necessary for the buoyancy resulting from this gradient to overcome the dissipative effects of viscous drag and heat diffusion. The gravitational potential energy liberated by the rising of lighter fluid and the sinking of heavier fluid must be greater than the energy dissipated by drag and diffusion. The relative importance of these effects can be expressed as a dimensionless ratio: the buoyant force divided by the product of the viscous drag and the rate of heat diffusion. The ratio is dimensionless in that all the units of measurement associated with the three quantities cancel exactly, leaving a pure number whose value is the same no matter what system of units is adopted. This ratio is called the Rayleigh number and defined by:

$$R = \frac{\alpha g d^3 (\Delta T)}{\kappa \nu} \tag{1.1}$$

where α is the thermal expansion coefficient, κ is the thermal diffusivity, ν is the kinematic viscosity, g is the acceleration due to gravity, d is the separation between the two plates and ΔT is the temperature difference. Convection begins when the Rayleigh number exceeds a critical value.

At the onset of convection, the flow in the fluid layer forms a regular pattern with regions of warm fluid going up and cool fluid going down. The pattern can be described in terms of a wavevector, which specifies the overall scale of a pattern but not its detailed from. The pattern actually observed depends on the geometry of the experimental apparatus. The patterns seen in the Rayleigh-Bénard configuration are roll-like, as shown in Figure 1.2. The fundamental unit of the pattern consists of two rolls that rotate in opposite

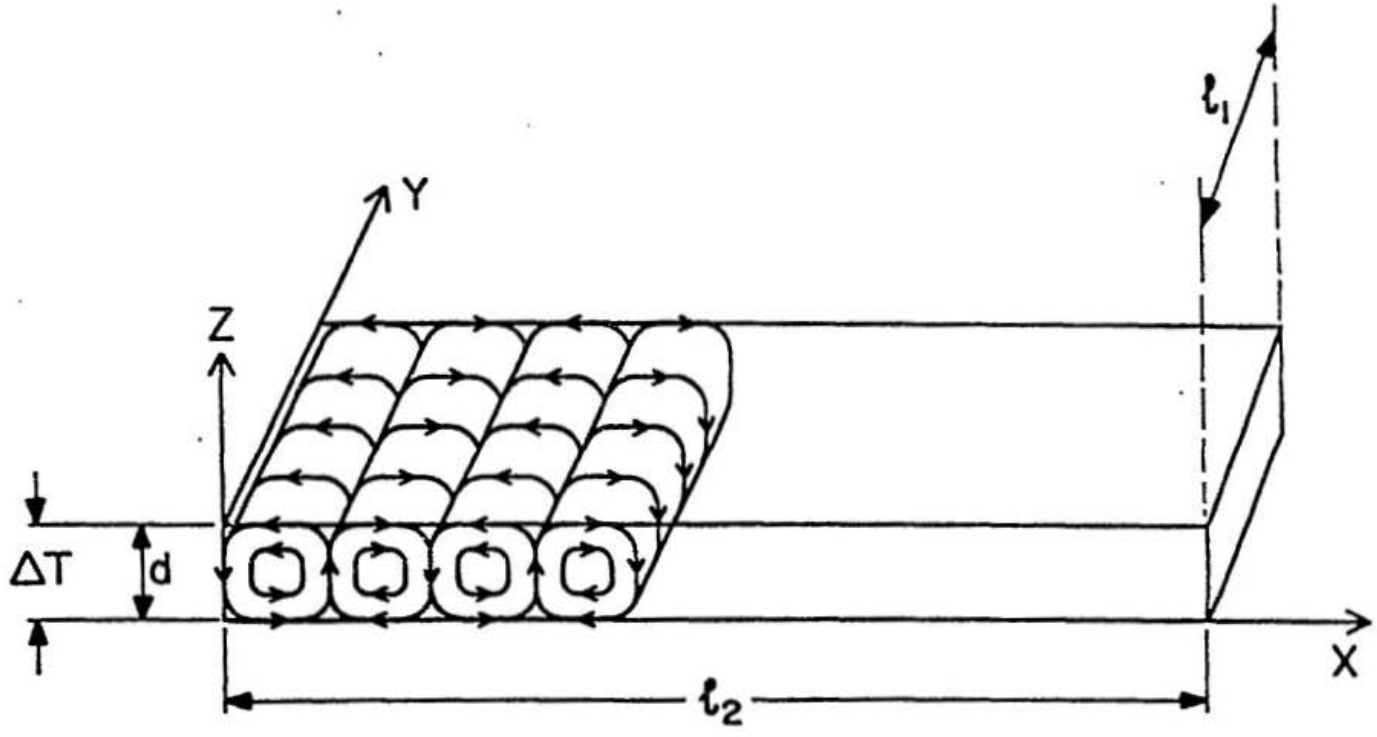

Figure 1.2: Roll-shaped cells are a stable configuration in convection in the Rayleigh-Bénard configuration. The fundamental unit of the pattern consists of two rolls that rotate in opposite directions. In a rectangular container the rolls are parallel to the shorter sides.

directions; the width of these two rolls forms one wavelength. In a rectangular container the rolls are parallel to the shorter sides.

When the convecting fluid is a binary liquid mixture instead of a pure liquid, the instability phenomena become richer. For example, with the proper choice of fluid parameters, the instability at the onset of convection could be oscillatory, *i.e.*, periodically time-dependent. A binary liquid mixture is an example of a double diffusive system, so called because there is a second diffusive field — the concentration field — in addition to the first diffusive field — the temperature field. The first double diffusive system considered in detail was a salt-water mixture, treated by Stommel *et al.* [3]. Later work by Hurle and Jakeman [4] extended the study to more general double diffusive systems where the temperature and concentration fields couple to each other. A nondimensional quantity, called the separation ratio, is defined as

$$\psi = \frac{\beta}{\alpha}\frac{\Delta c}{\Delta T} = -\frac{\beta}{\alpha}S_T c(1-c) \tag{1.2}$$

where β is the solutal expansion coefficient, c and Δc are the mean concentration of the mixture and the concentration difference across the fluid layer. S_T is the Soret coefficient, which characterizes the concentration gradient induced in the mixture by the applied temperature gradient. The value of the separation ratio of the binary fluid mixture determines whether the transition from the conduction state will be to an oscillatory convection state or to a stationary one.

To understand the richness of the possible instabilities in such systems, consider a salt-water mixture where both salinity and temperature increase upwards. While increasing salinity upwards makes the mixture more dense at the top and thus tends to destabilize the system, increasing temperature

upwards makes the mixture lighter at the top and tends to stabilize the system. Suppose that the system is in equilibrium initially. The question to ask is whether the equilibrium is stable or not. To test this, imagine a small quantity of solution being displaced upwards. The environment in its new position is warmer and more saline. In such a solution, the thermal diffusivity is much higher than the diffusivity of salt, so the temperature difference is quickly equalized, but the salinity difference remains. Hence the displaced packet rises still further, signalling an instability. Thus for double diffusive systems, convection can occur even when the temperature gradient is stabilizing. This is due to the very different time scales for thermal and mass diffusion. The ratio of these two time scales can be described by a dimensionless number, the Lewis number, defined as

$$L = D_m/\kappa \tag{1.3}$$

where D_m is the coefficient of mass diffusion.

Now consider a situation where the solution is hotter and more saline below. An upwardly displaced packet will meet an environment which is colder and less saline and, when the temperature is equalized by the rapid thermal diffusion, it will drop down because of its excess salinity. When it reaches its previous position it will still have the same salinity, but its temperature will be lower than the surroundings, and it will continue to fall until the excess salinity of the surroundings forces it back up. It will thus keep oscillating back and forth, signalling an oscillatory instability.

A binary liquid mixture is a more experimentally accessible example of a double diffusive system. It differs from the thermohaline (salt-water) system only in that, in the case of a binary mixture, a concentration gradient can be induced in the fluid by a temperature gradient through the Soret ef-

fect. Since the theoretical prediction of the onset of oscillatory convection by Hurle and Jakeman [4], a lot of work has been done on Rayleigh-Bénard convection in binary liquid mixtures. As the relevant parameters of the system are varied, a number of interesting phenomena have been observed, including forward and backward bifurcations to steady or time-dependent states [5], codimension-two bifurcations [6], time-dependent states including traveling wave (TW) convection [11, 15, 16], *etc.*

One quite interesting phenomenon revealed in studies of TW convection in binary fluid mixtures is the existence of a variety of confined states, in which TWs are observed in one spatial region of the experimental cell, while the rest of the fluid is motionless [7]-[10]. Several types of stable confined states have been discovered, both in rectangular cells, where the presence of endwalls can affect the dynamics, and in annular cells. The value of the separation ratio ψ has a strong effect on the nature of the states observed.

At the onset of convection with sufficiently negative value of ψ, the convection amplitude is observed to grow via a long transient to a state of slow-moving traveling waves [11]. If the reduced Rayleigh number $r \equiv R/R_c$, where R_c is the critical Rayleigh number for a pure fluid ($\psi = 0$) with the same properties as the mixture, is then decreased, this state of nonlinear traveling waves remains stable down to a saddle-node bifurcation back to conduction at $r = r^s$. If r is increased above onset, the TW phase speed decreases and eventually stops at a Rayleigh number denoted by r^*, and a stationary overturning convection (SOC) state results.

A convenient quantity for measuring the convection amplitude is the heat transfer through the convecting layer, which, written as a dimensionless ratio,

is the Nusselt number, defined as

$$N = \frac{Qd}{\lambda \Delta T}. \tag{1.4}$$

where Q is the total rate of heat transfer per unit area across the fluid layer, λ the thermal conductivity of the fluid and $\lambda \Delta T/d$ the rate of heat transfer per unit area when there is no convection. Thus $N = 1$ in the conduction state and $N > 1$ in convection states. Numerically calculated data for Nusselt number as a function of r for an ethanol-water mixture are shown in Figure 1.3 [13].

The TW state and the transition from TW to SOC have been considered in theoretical work [12] and numerical calculations [13, 14]. In reference [12], a perturbation expansion in ψ and $(r-1)$ around the convective state in a pure fluid is carried out, while the numerical work is a finite-difference integration of the Navier-Stokes equations. Both assume the Boussinesq approximation of the fluid equations and two-dimensional flow perpendicular to the roll axes. They impose rigid, impermeable boundary conditions at the upper and lower plates of the container, and periodic horizontal boundary conditions. Both the theory and the numerical calculations predict that the transition from TW and SOC should be continuous with no hysteresis at r^*, and that the phase speed should decrease close to r^* as $(r^* - r)^{1/2}$.

In experiments with a rectangular cell done by Walden *et al.* [11] and Moses *et al.* [15], the transition from TW to SOC was observed to be hysteretic, and the TW phase speed was reported to decrease linearly as a function of $r^* - r$. In a recent experiment by Ohlsen *et al.* [16], which was conducted in an annular cell with periodic boundary conditions, the transition was observed to be continuous within the experimental resolution of $\Delta r^*/r^* < 0.02\%$. Ohlsen *et al.* found that the TW phase velocity depended on Rayleigh number near r^*

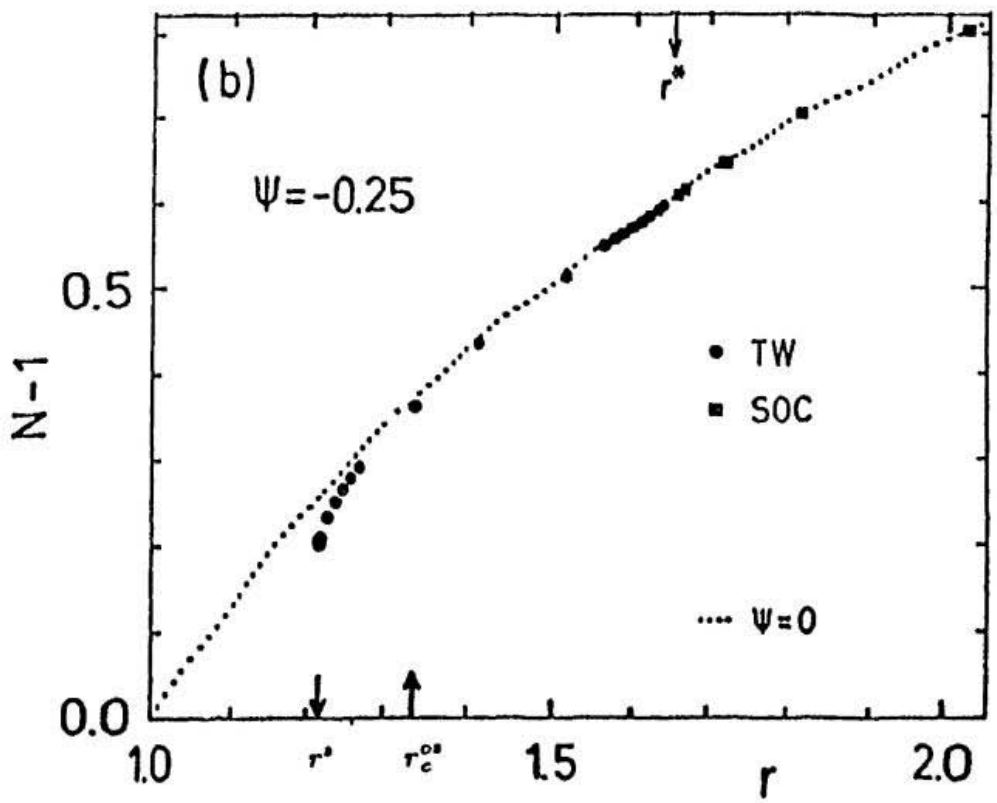

Figure 1.3: Numerically calculated Nusselt numbers as a function of r for TW and SOC states. Full symbols (small dots) refer to states in the mixture (pure fluid) that are stable under lateral periodic boundary conditions. At r^* the TW state loses stability to SOC, and at r^* the system undergoes a transition back to the conductive state. From [13].

like $(r^* - r)^b$, with $b \simeq 0.57$, reasonably close to the predicted value of $b = 0.5$.

The numerical calculations by Barten *et al.* [13, 14] also indicate that the linear concentration profile present in the conduction state is destroyed by convective mixing in the TW state. Thus, the vertical concentration gradient remains only in thin, horizontal boundary layers at the top and bottom of the fluid layer, and the fluid is well mixed in the interior of the rolls. Concentration from these boundary layers is fed into the upflow and downflow boundaries between the rolls, forming a lateral concentration wave. It is the phase difference between this lateral concentration field and the lateral temperature field which leads to traveling convection rolls. For sufficiently large convective amplitude, the concentration gradient due to the Soret effect is eliminated, and the resulting homogeneous fluid mixture exhibits the same stationary convective flow as a pure fluid.

Eaton *et al.* [17] studied the role of the concentration field in the TW state, using a combination of shadowgraph measurements and numerical calculations. They performed an experiment in an annular cell with an 8% by weight ethanol-water mixture. They visualized the convecting flow from the top of the cell using shadowgraphy, and compared their measurements with numerical results. They confirmed some predicted features of the symmetry and phasing of the TW concentration field.

In order to measure the lateral concentration distribution, which has been calculated numerically [13, 14], flow visualization from the side of the cell is needed. We have conducted experiments in a narrow rectangular cell, in which the width is much smaller than the length and the height. By viewing the cell from the side, lateral shadowgraph intensity profiles were recorded; these were then compared with numerical calculations. In choosing such a narrow rect-

angular cell, we attempt to obtain lateral shadowgraph intensity profiles with fewer optical effects in the direction of light propagation. This narrow geometry constrains the convection pattern to be quasi-one-dimensional. We thus refer to convection cell as quasi-one-dimensional. We studied the symmetry and phasing features of the concentration field in TW and SOC states. Our data appear to confirm some of the qualitative features of the numerical results but suggest significant quantitative differences, presumably due at least in part to the near-one-dimensionality of the experimental cell. In general however, our results suggest that a substantial improvement in our shadowgraph flow visualization is required before quantitative comparison can be made with the numerical predictions. There thus remains a lot of further work to be done on this matter.

In Chapter 2, a brief introduction to the linear stability analysis of Rayleigh-Bénard convection in a pure fluid and binary mixtures is given, and the numerical results of Barten *et al.* [13, 18] are discussed. Chapter 3 is a description of the experimental set-up and procedure. Experimental results are presented and discussed in Chapter 4. Chapter 5 contains a brief summary and conclusion. In an Appendix, some relevant properties of water-ethanol mixtures are tabulated.

Chapter 2

Theory

In this Chapter, an introduction to theories describing Rayleigh-Bénard convection is given. The starting point for theoretical studies is the linear stability analysis, which gives the critical Rayleigh number and wavelength at the onset of convection. Beyond the onset, nonlinear theory or direct numerical calculations have to be used to describe the system.

Following Chandrasekhar [19], Hurle and Jakeman [4] and Bhattacharjee [20], we first discuss the application of linear stability analysis to a pure fluid, then to a binary fluid mixture, including in each case a discussion of the stability criteria. Then we review the results of a nonlinear theory of binary mixture convection [12] and discuss the results of numerical calculations of TW states and SOC states [13, 14, 18].

In what follows, we consider a thin fluid layer confined between two horizontal plates. The distance between the two plates is d and the lateral dimension L is supposed to be infinity. We use Cartesian coordinates with the x-y plane

horizontal and the z axis pointing up, with $z = 0$ at the bottom plate. T_1 and c_1 denote the temperature and concentration of the fluid layer at the bottom plate and T_2 and c_2 the temperature and concentration of the fluid layer at the top plate. We always take the concentration to be that of the lighter component of the binary mixture; for our ethanol-water system, c denotes the concentration of ethanol.

2.1 Linear stability analysis for a pure fluid

2.1.1 Governing equations

The governing equations for thermal convection in a pure fluid can be found in many fluid dynamics text books [19]. The equation of continuity is

$$\frac{\partial \rho}{\partial t} + \nabla \cdot (\rho \vec{u}) = 0 \tag{2.1}$$

where ρ is the density and $\vec{u}$ the velocity of convecting flow. The equations of motion are the Navier-Stokes equations

$$\frac{\partial \vec{u}}{\partial t} + (\vec{u} \cdot \nabla)\vec{u} = -\frac{\nabla P}{\rho} + \vec{g} + \nu \nabla^2 \vec{u} \tag{2.2}$$

where P is the pressure, g the gravitational acceleration and ν the kinematic viscosity. The temperature field T satisfies

$$\frac{\partial T}{\partial t} + (\vec{u} \cdot \nabla)T = \kappa \nabla^2 T \tag{2.3}$$

where κ is the thermal diffusivity. The steady, conductive state with

$$\vec{u} = 0, \tag{2.4}$$

$$T = T_1 + \frac{T_2 - T_1}{d} z = T_1 - \frac{\Delta T}{d} z \tag{2.5}$$

and

$$\frac{\nabla P}{\rho} = \vec{g} \tag{2.6}$$

is always a solution of eqs. (2.1 - 2.3). To find out whether this solution is stable or not, we add small perturbations $\delta\vec{u}$, δT and δP to the steady conduction solution and study the equations governing the time development of the perturbations. If the perturbations decay exponentially in time, then the unperturbed state is stable. If, on the other hand, the perturbations grow with time, then the original state is unstable against the perturbation and an instability sets in.

In general, the density of the fluid is a function of temperature and we can write

$$\rho = \rho_0[1 - \alpha(T - T_0)] \tag{2.7}$$

where $\alpha = -\frac{1}{\rho}\frac{\partial \rho}{\partial T}$ is the thermal expansion coefficient and T_0 is the temperature at which $\rho = \rho_0$. To simplify the equations, we apply the Boussinesq approximation [21], which sets ρ equal to ρ_0 everywhere except in the coefficient of $\vec{g}$ and treats the other fluid properties as constants. For an incompressible fluid, the continuity equation (2.1) becomes

$$\nabla \cdot \vec{u} = 0. \tag{2.8}$$

Using the Boussinesq approximation, we can linearize eqs. (2.2) and (2.3) in the small perturbations $\delta\vec{u} = (u_x, u_y, u_z)$, δT and δP about the conduction state. After using eq. (2.8), we find the equations governing δT and u_z to be

$$(\frac{\partial}{\partial t} - \kappa\nabla^2)\delta T = u_z\frac{\Delta T}{d} \tag{2.9}$$

and

$$\nabla^2(\frac{\partial}{\partial t} - \nu\nabla^2)u_z = \alpha g(\frac{\partial^2}{\partial x^2} + \frac{\partial^2}{\partial y^2})\delta T. \tag{2.10}$$

We now scale all lengths by d, time by d^2/ν, temperature by ΔT and velocity by κ/d. The dimensionless quantities are $(X, Y, Z) = (x, y, z)/d$, $\tau = t\nu/d^2$, $\theta = \delta T/\Delta T$ and $w = u_z d/\kappa$. Eqs. (2.10) and (2.9) then become

$$\nabla^2(\frac{\partial}{\partial \tau} - \nabla^2)w = R(\frac{\partial^2}{\partial X^2} + \frac{\partial^2}{\partial Y^2})\theta \tag{2.11}$$

and

$$(\sigma\frac{\partial}{\partial \tau} - \nabla^2)\theta = w \tag{2.12}$$

where

$$\sigma = \nu/\kappa \tag{2.13}$$

is a dimensionless ratio called Prandtl number and R, the Rayleigh number, was defined in eq. 1.1. We now seek solutions to the above equations which correspond to the formation of convection rolls. Such rolls are characterized by a two-dimensional wavenumber in the X-Y plane with components k_X and k_Y and hence the solutions will be of the form

$$\theta(X, Y, Z, \tau) = \Theta(Z)e^{i(k_X X + k_Y Y) + p\tau}, \tag{2.14}$$

$$w(X, Y, Z, \tau) = W(Z)e^{i(k_X X + k_Y Y) + p\tau}. \tag{2.15}$$

Substituting these forms into eqs. (2.11) and (2.12), we get

$$(D^2 - a^2)(D^2 - a^2 - p)W = Ra^2\Theta \tag{2.16}$$

$$(D^2 - a^2 - \sigma p)\Theta = -W \tag{2.17}$$

with $D = \frac{d}{dZ}$ and a, the dimensionless wavenumber, given by

$$a^2 = k_X^2 + k_Y^2. \tag{2.18}$$

Eqs. (2.16) and (2.17) are eigenvalue equations for the growth rate p. If $Re(p) < 0$, the fluctuations decay to zero as $t \to \infty$ and the initial state is

stable. If, however, $Re(p) > 0$, the perturbations grow in time and the initial conduction state is unstable against the formation of rolls.

We now consider the boundary conditions for $W(Z)$ and $\Theta(Z)$. Since the temperatures of the top and bottom plates are held constant, the temperature perturbations vanish at $Z = 0$ and $Z = 1$. Since the plates are stationary, we must have $W = 0$ at $Z = 0$ and $Z = 1$. If the plates are rigid, then the X and Y components of the dimensionless velocity fields (u and v respectively) also vanish at the boundaries. This implies that $\frac{\partial u}{\partial X}$ and $\frac{\partial v}{\partial Y}$ are zero on the surfaces and the continuity condition leads to $\frac{\partial W}{\partial Z} = 0$ at $Z = 0$ and $Z = 1$. Thus the rigid-rigid boundary conditions are

$$W = DW = \Theta = 0 \qquad Z = 0, 1. \tag{2.19}$$

For analytic calculations it is often convenient to assume free boundaries. This implies that there are no stresses on the horizontal surfaces, leading to

$$\frac{\partial u}{\partial Z} = -\frac{\partial w}{\partial X} = 0 \tag{2.20}$$

and

$$\frac{\partial v}{\partial Z} = -\frac{\partial w}{\partial Y} = 0 \tag{2.21}$$

at $Z = 0$ and $Z = 1$, since on the plates, $w = 0$ independent of X and Y. The continuity equation now yields

$$D^2 W = 0. \tag{2.22}$$

Thus the free boundary conditions are

$$W = D^2 W = \Theta = 0 \qquad Z = 0, 1. \tag{2.23}$$

2.1.2 Stability criteria

For the free boundary conditions (2.23), it is immediately clear that solutions of eqs. (2.16) and (2.17) can be written as

$$W = A_n \sin(n\pi Z) \tag{2.24}$$

$$\Theta = B_n \sin(n\pi Z) \tag{2.25}$$

where n is an integer. Self-consistent determination of the coefficients A_n and B_n leads to the eigenvalue equation

$$\begin{vmatrix} (n^2\pi^2 + a^2)^2 + p(n^2\pi^2 + a^2) & -Ra^2 \\ 1 & -(n^2\pi^2 + a^2) - \sigma p \end{vmatrix} = 0. \tag{2.26}$$

It can be shown [19] that, for a pure fluid, the imaginary part of p will be zero if the real part is zero. To obtain the critical value of R, we set $p = 0$ and find

$$R_0 = \frac{(n^2\pi^2 + a^2)^3}{a^2}. \tag{2.27}$$

It is clear from the roots of the quadratic in p (Eq. (2.26)) that for $R < R_0$, p is always negative and hence the perturbations decay in time, while for $R > R_0$, p is positive, leading to instability. The critical value R_c of R is now determined by finding the minimum of R_0. We take $n = 1$ and minimize the resulting R_0 with respect to a. This leads to

$$R_c = \frac{27\pi^4}{4} \tag{2.28}$$

and

$$a_c^2 = \frac{\pi^2}{2}. \tag{2.29}$$

Thus we have found the value of the Rayleigh number at which convection begins, and the wavelength of the convection cells. Notice that the theory

does not tell us what the shape of the cells will be — that is determined by the X and Y components of the wavevector. The critical Rayleigh number is determined by the magnitude of the wavenumber alone.

In an actual laboratory experiment, the rigid boundary conditions are the correct ones, so we really need to find R_c for the boundary conditions given in Eq. (2.19). With these boundary conditions, solution of the equations is more involved and ultimately R_c and a_c must be determined numerically. The results are [19]

$$R_c \simeq 1708 \tag{2.30}$$

and

$$a_c \simeq 3.117, \tag{2.31}$$

significantly different from the free boundary values of Eqs. (2.28) and (2.29). Thus instability occurs if and only if $R > 1708$, and the horizontal wavelength of the disturbance at the onset of instability is $2\pi d/a_c = 2.016d$. The experimental data are in good agreement with the above values of R_c and a_c [22][23].

2.2 Binary fluids

In binary fluid systems, the first instability can be either stationary or oscillatory. Binary fluid systems are similar to the thermohaline system discussed in Chapter 1, except for the fact that in binary mixtures a temperature difference can drive a mass current through the Soret effect [24, 25]. Thus a concentration gradient can be established. Since the density of a binary fluid depends on concentration as well as temperature, even small vertical concentration gradients can have a profound effect on the hydrodynamic stability of

these systems.

In this section, the Soret effect is discussed, then the linear stability analysis and stability criteria for the binary fluid systems are presented, for the most part following the treatments of Hurle and Jakeman [4] and Bhattacharjee [20].

2.2.1 The Soret effect

The equations relating the flux of heat ($\vec{J}_Q$) and matter ($\vec{J}_c$) to the temperature and concentration gradients in a binary fluid mixture can be written as [24, 25]

$$\vec{J}_Q = -\lambda \nabla T \tag{2.32}$$

$$\vec{J}_c = -\rho D_m [S_T c(1-c)\nabla T + \nabla c] \tag{2.33}$$

where D_m is the mass diffusion constant, λ the thermal conductivity and S_T the Soret coefficient. Here, the contribution of the concentration gradient to the heat flux — known as the Dufour effect — is neglected. In liquids, this effect is much smaller than the Soret effect.

It is clear from (2.33) that a redistribution of concentration can be induced in a two-component fluid by changing the temperature distribution. This redistribution is governed by the equations

$$\frac{\partial T}{\partial t} = \frac{\lambda}{\rho c_p} \nabla^2 T \tag{2.34}$$

and

$$\frac{\partial c}{\partial t} = D_m [S_T c(1-c)\nabla^2 T + \nabla^2 c], \tag{2.35}$$

where c_p is the specific heat of the mixture at constant pressure, and, consistent with the Boussinesq approximation, we have neglected the spatial variation of the coefficients of ∇c and ∇T in (2.32) and (2.33). For a mixture at rest in

the Bénard configuration (confined between two horizontal plates and subject to a uniform vertical temperature gradient) (2.34) and (2.35) reduce to the single equation

$$\frac{\partial c}{\partial t} = D_m \frac{\partial^2 c}{\partial z^2}. \tag{2.36}$$

The boundary conditions are determined from the relation (2.33). If the confining plates are impervious so that $\vec{J}_c$ vanishes there, we obtain the boundary condition

$$S_T c(1-c)\frac{\partial T}{\partial z} + \frac{\partial c}{\partial z} = 0. \tag{2.37}$$

A concentration gradient is therefore established at the boundaries, and this will extend at a rate governed by the diffusion equation (2.36) through the entire fluid. For a layer of depth d the characteristic mass diffusion time involved is

$$\tau_m = \frac{d^2}{D_m}. \tag{2.38}$$

The final stationary state, in which (2.37) holds throughout the mixture, is reached after times which are long compared to τ_m.

The Soret effect is thus a mechanism by which an applied temperature gradient can establish a concentration gradient in a binary liquid mixture even though it is confined by impervious walls.

2.2.2 Governing equations

For binary fluid systems, another equation describing the concentration c, in addition to the equations required to describe the pure fluid, is required. The governing equations are

$$\frac{\partial \rho}{\partial t} + \nabla \cdot (\rho \vec{u}) = 0 \tag{2.39}$$

$$\frac{\partial \vec{u}}{\partial t} + (\vec{u} \cdot \nabla)\vec{u} = -\frac{\nabla P}{\rho} + \vec{g} + \nu \nabla^2 \vec{u} \tag{2.40}$$

$$\frac{\partial T}{\partial t} + (\vec{u} \cdot \nabla)T = \kappa \nabla^2 T \tag{2.41}$$

$$\frac{\partial c}{\partial t} + (\vec{u} \cdot \nabla)c = D_m \nabla^2 c + D_m S_T c(1-c)\nabla^2 T. \tag{2.42}$$

The conduction state is characterized by

$$\vec{u} = 0 \tag{2.43}$$

$$T = T_1 - \frac{\Delta T}{d} z \tag{2.44}$$

$$c = c_1 - \frac{\Delta c}{d} z \tag{2.45}$$

where Δc must satisfy

$$\frac{\Delta c}{\Delta T} = -S_T c(1-c). \tag{2.46}$$

We again consider perturbations $\delta \vec{u} = (u_x, u_y, u_z)$, δP, δT and δc about the conduction state. In this case the density ρ varies with both temperature and concentration, and can be written as

$$\rho = \rho_0[1 - \alpha(T - T_0) - \beta(c - c_0)] \tag{2.47}$$

where $\beta = -\frac{1}{\rho}\frac{\partial \rho}{\partial c}$ is the solutal expansion coefficient and $\rho_0 = \rho(T_0, c_0)$. Applying the Boussinesq approximation, the linearized equations for small perturbations $u_z, \delta T$ and δc now become

$$\nabla^2(\frac{\partial}{\partial t} - \nu \nabla^2)u_z = -\frac{g}{\rho_0}(\frac{\partial^2}{\partial x^2} + \frac{\partial^2}{\partial y^2})\delta \rho, \tag{2.48}$$

$$(\frac{\partial}{\partial t} - \kappa \nabla^2)\delta T = u_z \frac{\Delta T}{d} \tag{2.49}$$

and

$$(\frac{\partial}{\partial t} - D_m \nabla^2)\delta c = u_z \frac{\Delta c}{d} + D_m S_T c(1-c)\nabla^2 \delta T. \tag{2.50}$$

Using dimensionless variables defined by $(X, Y, Z) = (x, y, z)/d$, $\tau = t\nu/d^2$, $\theta = \delta T/\Delta T$, $w = u_z d/\kappa$ and $\phi = \delta c/\Delta c$ leads to the dimensionless equations

$$\nabla^2(\frac{\partial}{\partial \tau} - \nabla^2)w = R(\frac{\partial^2}{\partial X^2} + \frac{\partial^2}{\partial Y^2})\theta + \psi R(\frac{\partial^2}{\partial X^2} + \frac{\partial^2}{\partial Y^2})\phi \tag{2.51}$$

$$(\sigma\frac{\partial}{\partial \tau} - \nabla^2)\theta = w \tag{2.52}$$

$$(\frac{\sigma}{L}\frac{\partial}{\partial \tau} - \nabla^2)\phi = \frac{w}{L} - \nabla^2\theta \tag{2.53}$$

where $L = D_m/\kappa$ is the Lewis number, and ψ the separation ratio defined in eq. (1.2). As before, we consider perturbations of the form

$$\begin{pmatrix} w(X, Y, Z) \\ \theta(X, Y, Z) \\ \phi(X, Y, Z) \end{pmatrix} = \begin{pmatrix} W(Z) \\ \Theta(Z) \\ \Phi(Z) \end{pmatrix} e^{i(k_X X + k_Y Y)} e^{p\tau}. \tag{2.54}$$

Inserting eqs. (2.54) in eqs. (2.51), (2.52) and (2.53) we arrive at

$$(D^2 - a^2)(D^2 - a^2 - p)W = Ra^2\Theta + \psi Ra^2\Phi \tag{2.55}$$

$$(D^2 - a^2 - \sigma p)\Theta = -W \tag{2.56}$$

$$(D^2 - a^2 - \frac{\sigma}{L}p)\Phi = -\frac{W}{L} + (D^2 - a^2)\Theta \tag{2.57}$$

where $a^2 = k_X^2 + k_Y^2$ as before.

The boundary conditions need to be discussed next. For the velocity, free boundary conditions imply $W = D^2W = 0$ at $Z = 0, 1$, while rigid boundaries would require $W = DW = 0$ at $Z = 0, 1$. The temperature is prescribed on the boundaries, which have high conductivities, hence we take $\Theta = 0$ at $Z = 0, 1$. The idealization for the concentration field is to have $\Phi = 0$ on $Z = 0, 1$. The realistic boundary condition is, however, to have the normal current vanish, i.e., from (2.37) $D[c+S_T c(1-c)T] = 0$. In terms of the dimensionless perturbed

variables this becomes $D(\Phi - \Theta) = 0$ at the boundaries $Z = 0, 1$. The two classes of boundary conditions are thus

i) Idealized (free-pervious):

$$W = D^2W = \Theta = \Phi = 0 \qquad \text{on the boundaries,} \tag{2.58}$$

ii) Realistic (rigid-impervious):

$$W = DW = \Theta = D(\Phi - \Theta) = 0 \qquad \text{on the boundaries.} \tag{2.59}$$

2.2.3 Stability criteria

For the idealized boundaries (2.58), eqs. (2.55), (2.56) and (2.57) may be solved exactly. In this case the solution for W, Θ and Φ will be of the form $\sin(n\pi z)$, with $n = 1$ giving the critical Rayleigh number as before. For consistent determination of the coefficients of $\sin(\pi z)$ in the functions W, Θ and Φ from eqs. (2.55), (2.56) and (2.57), we must have

$$\begin{vmatrix} (\pi^2 + a^2)(\pi^2 + a^2 + p) & -Ra^2 & -\psi Ra^2 \\ -1 & \pi^2 + a^2 + \sigma p & 0 \\ -\frac{1}{L} & -(\pi^2 + a^2) & \pi^2 + a^2 + \frac{\sigma}{L}p \end{vmatrix} = 0. \tag{2.60}$$

For the stationary bifurcation, $p = 0$, we find

$$R^{sc} = \frac{(\pi^2 + a^2)^3}{a^2} \frac{1}{1 + \psi(1 + \frac{1}{L})}. \tag{2.61}$$

Minimization of this with respect to a^2 yields as before $a_c^2 = \frac{\pi^2}{2}$ and

$$R_c^{sc} = \frac{27\pi^4}{4} \frac{1}{1 + \psi(1 + \frac{1}{L})}. \tag{2.62}$$

For this system, a Hopf bifurcation to an oscillatory state is also possible. In this case, two of the roots are of the form $p = \pm i\omega$ and this yields, from the real and imaginary parts,

$$\frac{\sigma^2\omega^2}{(\pi^2+a^2)^2} = \left[\sigma(1+L) + L - \frac{\sigma a^2 R(1+\psi)}{(\pi^2+a^2)^3}\right] \tag{2.63}$$

and

$$\frac{\sigma^2\omega^2}{(\pi^2+a^2)^2} = \frac{L\sigma}{1+\sigma+L}\left[1 - \frac{Ra^2(\psi+\frac{\psi}{L}+1)}{(\pi^2+a^2)^3}\right]. \tag{2.64}$$

Eliminating ω from these equations leads to an expression for the critical Rayleigh number R^{os},

$$R^{os} = \frac{(\pi^2+a^2)^3}{a^2}\frac{(1+L)(1+\sigma)(\sigma+L)}{\sigma[1+\sigma(1+\psi)]}. \tag{2.65}$$

Minimizing with respect to a^2 yields

$$R_c^{os} = \frac{27\pi^4}{4}\frac{(1+L)(1+\sigma)(\sigma+L)}{\sigma[1+\sigma(1+\psi)]} \tag{2.66}$$

with $a_c^2 = \frac{\pi^2}{2}$, and

$$\omega_c = \frac{3\pi^2}{2\sigma}\left[-\frac{\psi(1+L)(\sigma+L)}{1+\sigma(1+\psi)} - L^2\right]^{1/2}. \tag{2.67}$$

The stationary and Hopf bifurcations coalesce at a point called the co-dimension-two point, $\psi = \psi_c$, where $\omega = 0$ and $R^{os} = R^{sc}$. From eqs. (2.63) and (2.64), the separation ratio ψ_c at the co-dimension two point is

$$\psi_c = -\frac{(1+\sigma)}{(1+\frac{1}{L})(1+\frac{\sigma}{L})+\sigma}. \tag{2.68}$$

The convection will be oscillatory if $R^{os} < R^{sc}$ and stationary otherwise. In principle, ψ is not restricted in magnitude or sign. The relations (2.62) and (2.66) are plotted in figure 2.1 for a wide range of ψ and taking $\sigma = 10$ and $L = 10^{-2}$, appropriate to water-like mixtures. Only curve (a) in figure 2.1

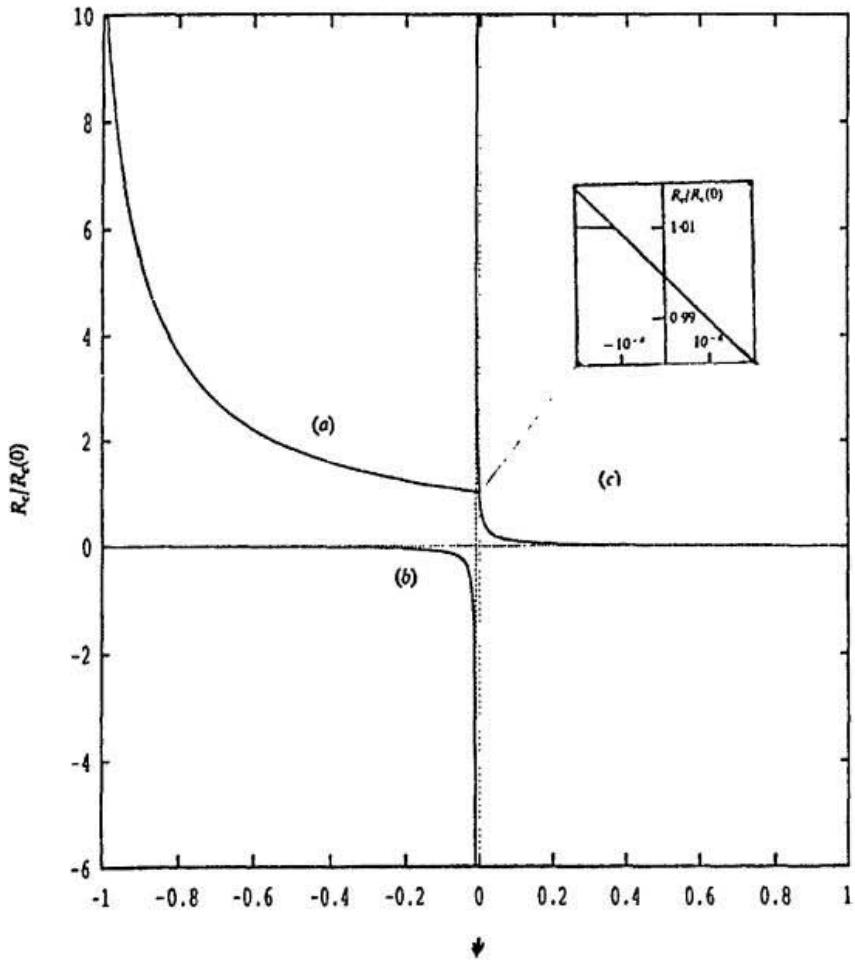

Figure 2.1: R_c vs. ψ for binary fluid mixture systems with free-pervious boundaries. ($R_c(0) = 27\pi^4/4$.) (a), time-dependent solution; (b) and (c), stationary convection. The inset shows detail in the region $R_c/R_c(0) \sim 1$, $\psi \sim 0$. From [4].

corresponds to the onset of time dependent motion. The detailed behaviour near $\psi = 0$ is shown in the inset. For positive Rayleigh numbers (destabilizing temperature gradients) time-dependent motions are restricted to the region

$$-\frac{\sigma+1}{\sigma} < \psi < -\frac{(1+\sigma)}{(1+\frac{1}{L})(1+\frac{\sigma}{L})+\sigma}. \tag{2.69}$$

When this inequality is satisfied, the first kind of instability to set in is oscillatory since $R_c^{os} < R_c^{sc}$.

There is also an asymptote in the R_c^{sc} versus ψ curve at $\psi = -\frac{1}{1+1/L}$ (shown as a dotted line in figure 2.1) below which stationary convection occurs when the applied temperature gradient is stabilizing (i.e., heating from above). The strong destabilizing effect of the concentration gradient in such circumstances, and also when ψ is positive for destabilizing temperature gradients, shows up in the extremely small values taken by R_c^{sc} (curves (b) and (c)). Note that when $\psi < -\frac{1}{1+1/L}$, the system is unstable to both positive and negative temperature gradients.

For the realistic boundary conditions (2.20), the problem is not analytically solvable for arbitrary ψ and L. The stability graph obtained from approximate or exact numerical solutions is qualitatively similar to that of Figure 2.1 for idealized boundaries [4, 26, 27].

2.3 Nonlinear theory

A linear stability analysis of the conducting states correctly predicts the critical Rayleigh number and the existence of a Hopf bifurcation at the onset of convection for binary fluids. Beyond the onset, nonlinear theory has to be taken into account to describe the system. By a nonlinear expansion around

the conducting state of a binary fluid, the dynamical behaviour of the convection state around the onset has been studied [28]-[30]. Such an expansion is only valid near the co-dimension-two point, where the convective flow does not destroy the linear concentration profile.

Considering the effect of convective mixing of concentration, Bensimon *et al.* [12] have recently developed a nonlinear theory and presented results relevant to the experiments done at values of $\psi \ll \psi_c$. In their theory, they treated the separation ratio ψ as a small parameter, and analyzed convection in binary mixtures by an expansion around the pure fluid convective state instead of the binary mixture conducting state. The temperature and velocity fields were assumed to have the same form, though not necessarily the same amplitude, as in a pure fluid. The equation for the concentration field was solved analytically in two limits: for TW velocity $v_p \gg |\vec{u}|$, the velocity of the convective flow, which corresponds to the regime near the transition from conductive state to TW state, and $v_p \ll |\vec{u}|$, which is in the regime near the transition from TW to SOC. In between these two limits, the concentration field was determined numerically.

For rigid-impermeable boundaries, they determined the amplitude of convection cA (Figure 2.2) and the TW velocity v_p (Figure 2.3) as a function of the reduced temperature difference $\epsilon^2 = (R - R_c)/R_c$. The lower branch of the amplitude in Figure 2.2 corresponds to fast and unstable TW solutions, the upper one to slow, stable ones. The TW phase velocity decreases quickly as ϵ is increased on the upper branch of slow TW. Their results predicted a continuous transition from the TW state to the SOC state as shown in the inset of Figure 2.3.

For the unstable fast TW states, the concentration profile deviates only

slightly from the linear gradient existing in the conductive state (Figure 2.4), while for the stable slow TW states, the concentration profile exhibits clear boundary layers (Figure 2.5). In this case, the concentration gradients are confined to the boundary layers near the walls (where the flow velocity vanishes), and to the free boundary layers along the vertical separations of adjacent rolls.

2.4 Some numerical results for ethanol-water mixtures

Recently, Barten *et al.* [13, 14, 18] have numerically studied the TW and SOC states in ethanol-water systems. They used a finite-difference method to solve the basic hydrodynamic equations in the Boussinesq approximation. They considered a system infinitely large in the y direction (along the roll axes) and applied periodic boundary conditions in the x direction (perpendicular to the roll axes) and realistic vertical boundary conditions as discussed in section 2.2. These numerical results are briefly reviewed here and will be used to compare with our experimental data in Chapter 4.

Figure 2.6 is the numerically calculated Nusselt number for nonlinear SOC and TW convective states as a function of r for $\psi = -0.25$, corresponding to an 8% ethanol-water mixture at a temperature of 27°C, as well as for SOC in a pure fluid corresponding to $\psi = 0$. The frequency of the TW monotonically decreases from its Hopf value at r_c^{os} until the TW merges nonhysteretically, and with vanishing frequency, with the SOC branch at r^*. Close to r^*, a square-root variation of the frequency, $\omega \simeq 1.3(r^* - r)^{1/2}$, is found. If r is decreased from r_c^{os} to the saddle point at r^s, the TW state undergoes a discontinuous

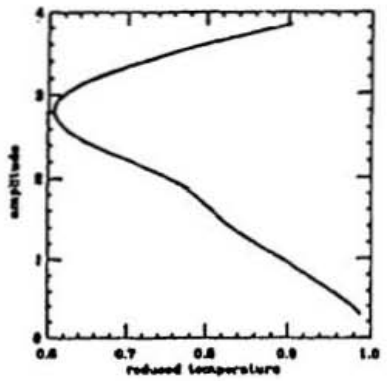

Figure 2.2: The reduced amplitude of convection ϵA as a function of the reduced temperature $\epsilon^2/|\psi|$ for $L = 0.01$ and $\psi = -0.25$, in the case of rigid-impermeable boundary conditions. The lower branch corresponds to fast (and unstable) TW solutions, the upper one to slow and stable ones. From [12].

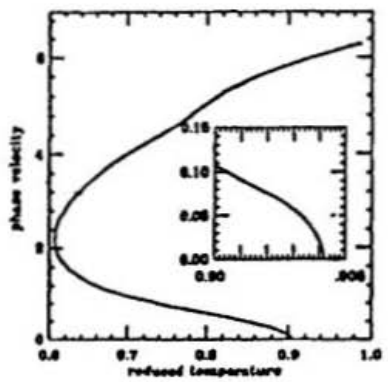

Figure 2.3: The reduced phase velocity of the traveling waves $v_p\sqrt{-\psi}$ as a function of the reduced temperature $\epsilon^2/|\psi|$ for $L = 0.01$ and $\psi = -0.25$, in the case of rigid-impermeable boundary conditions. The inset is a magnification of the critical point where the TW convection goes into the SOC state. The transition is continuous. From [12].

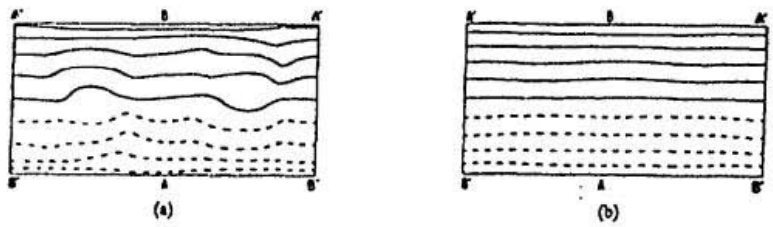

Figure 2.4: Isoconcentration lines for various unstable solutions for $L = 0.01$ and $\psi = -0.25$, (a) $\epsilon^2/|\psi| = 0.700$ and (b) $\epsilon^2/|\psi| = 0.850$. From [12].

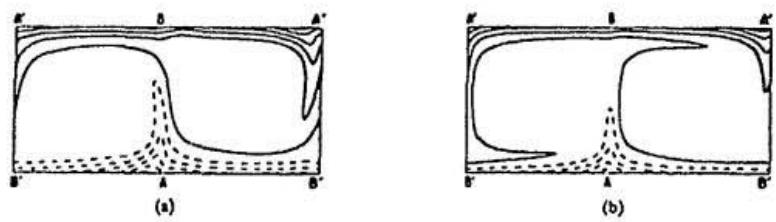

Figure 2.5: Isoconcentration lines for various stable solutions for $L = 0.01$ and $\psi = -0.25$, (a) $\epsilon^2/|\psi| = 0.700$ and (b) $\epsilon^2/|\psi| = 0.850$. From [12].

transition back to the conductive state.

An r-ψ phase diagram is shown in Figure 2.7, which illustrates the existence range of stable conductive and nonlinear convective states in the ethanol-water system. The double logarithmic plot was used to resolve details at small ψ and $r-1$. The conductive state is stable below the oscillatory critical Rayleigh number r_c^{os}. In the ψ range of Figure 2.7 TWs bifurcate at r_c^{os} if we increase r from the conduction state. For large negative ψ the upper existence boundary of the TW state, r^*, moves to larger and larger values. For less negative ψ, the existence range of stable TWs shrinks to zero as r^s and r^* come together.

Figure 2.8 shows the structural changes of rolls in the TW and SOC states as r is increased from r^s to r^* and beyond onto the SOC state. After transients have died out, the TW convective fields have the form of waves traveling to the right: $F = F(x - v_p t, z)$ where $v_p = \omega/k$ is the phase velocity. With the resolution of Figure 2.8, the velocity fields of TW and SOC roll patterns look similar to each other and to those found for a pure fluid. With increasing r, convection intensifies and warm upflow (cold downflow) bends the initially horizontal isotherms more and more upwards (downwards). In the TW state, however, the extrema of the isotherms do not coincide with those of the vertical velocity field: the temperature wave lags behind the w-velocity wave. Also, the concentration wave is phase shifted relative to the temperature wave and the w-wave. These phase differences monotonically decrease as the TW frequency decreases.

Note that the concentration wave is highly anharmonic. It is the TW concentration field that shows the most pronounced structure. Furthermore its changes when approaching the SOC state at r^* are most conspicuous. To understand these properties, one has to keep in mind that convection mixes the

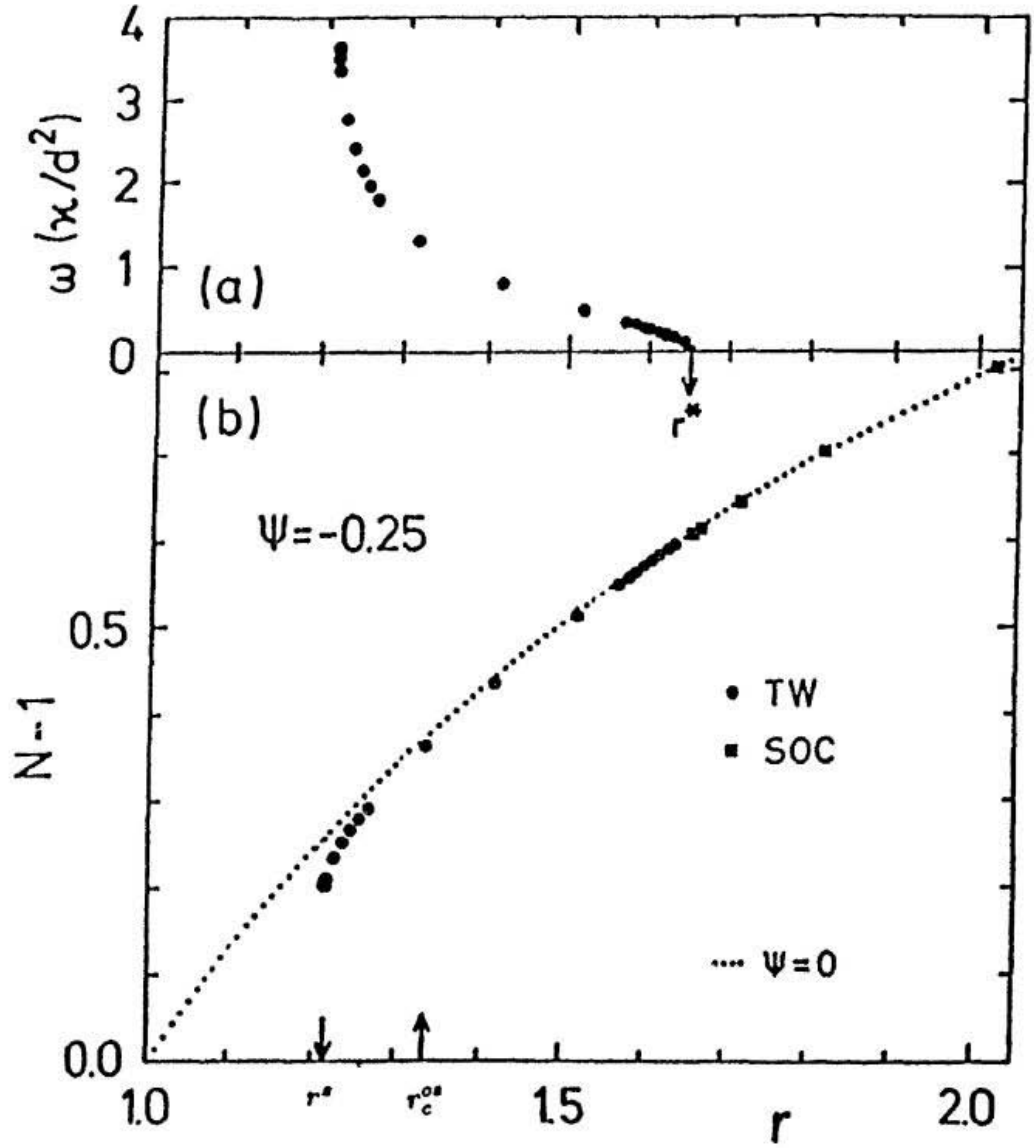

Figure 2.6: Numerically obtained bifurcation properties of nonlinear convective states. a) Frequency of stable TW and b) Nusselt number vs. r. Full symbols (small dots) refer to states in the mixture (pure fluid) that are stable under lateral periodic boundary conditions. At r^* the TW merges nonhysteretically and with zero frequency with the SOC branch. The calculations were done for $L = 0.01$, $\sigma = 10$, $\psi = -0.25$, $r_c^{os}(k = \pi) = 1.33$, $\omega_H(k = \pi) = 11.2$, $r^s \simeq 1.21$, $r^* \simeq 1.65$. From [13].

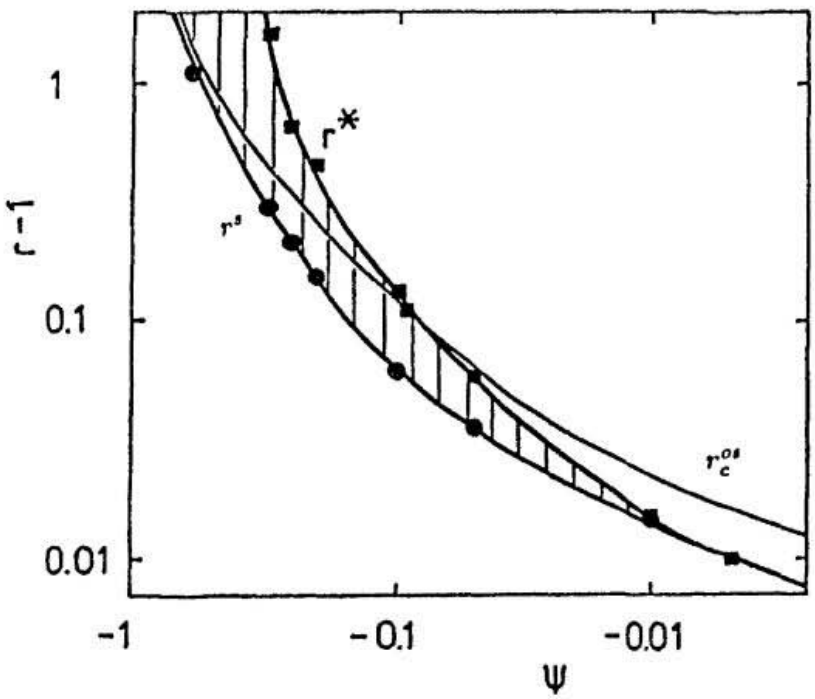

Figure 2.7: Boundaries of stable states in a double-logarithmic $r-1$ vs. ψ phase diagram (parameters as in Figure 2.6). The symbols show calculated points and full lines are guides to the eye. The conductive state is stable below r_c^{os}. TWs are stable in the region between the saddle node at r^s and r^*. From [13].

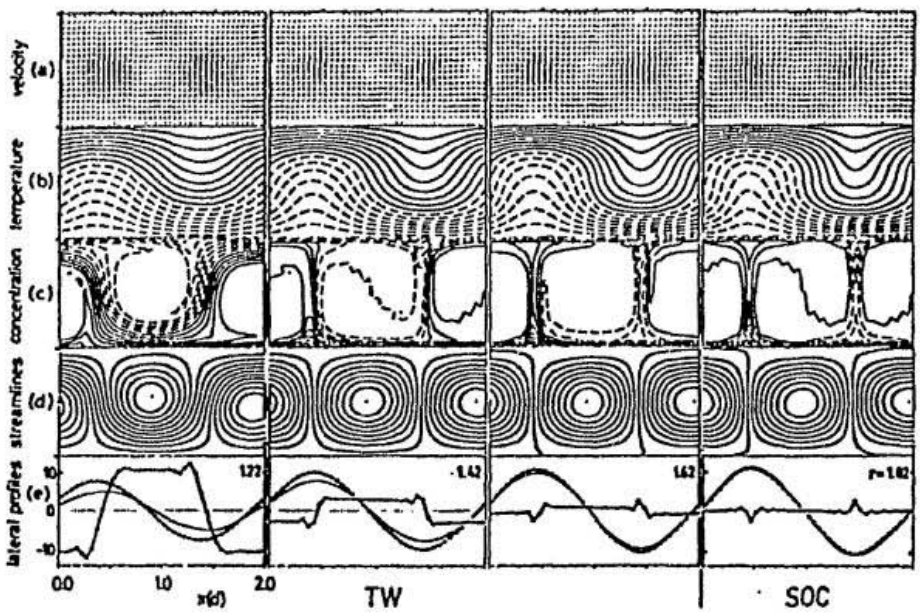

Figure 2.8: Structural properties of TW and SOC convective states: velocity field (a), equidistant isolines of the temperature (b) and concentration (c) field, streamlines (d) (for TWs in the frame comoving with the phase velocity to the right), and lateral profiles (e) at midheight, $z = 1/2$, of w (thin line), $40(T - T_0)$ (triangles), and $400(c - c_0)$ (squares). The first three columns represent TWs traveling to the right. The first one at $r = 1.22$ with frequency $\omega \simeq 0.3\omega_H$ is close to the saddle, $r^s \simeq 1.21$. For the second one $\omega \simeq 0.07\omega_H$. The last one at $r = 1.62$ is close to $r^* \simeq 1.65$ with $\omega \simeq 0.02\omega_H$. The SOC state at $r = 1.82$ is well beyond the transition point r^*. From [13].

fluid and destroys the conductive state's Soret induced concentration gradient between the top and bottom of the layer. In fact, in the SOC state where the streamlines of the velocity field are closed, the alcohol is practically homogeneously distributed at the mean concentration level over the bulk of the fluid. Only in the two narrow top and bottom boundary layers, the width of which decreases with increasing convection intensity, is there an almost linear concentration variation with z. At the positions of maximal up and down flow these boundary layers are slightly deformed into the bulk.

The symmetry properties of the fluid fields are also quite distinct in the different states. In the conductive state the deviations of all fields from their mean are invariant under lateral translation and are symmetric under reflection through the midplane of the layer, $z = 1/2$. SOC in mixtures, as well as in the pure fluid, breaks both symmetries, but there is a lateral periodicity and reflection symmetry between rolls of opposite vorticity. While a TW also has the lateral periodicity, the reflection symmetries presented in the SOC state are broken.

These numerical results will be compared with our experimental results in Chapter 4.

Chapter 3

Experimental Apparatus and Procedure

In this Chapter, the general experimental set-up and procedures are described. The central component of our experiment is the convection cell, a narrow rectangular cell which constrains the convection pattern to be quasi-one-dimensional. Accurate thermal measurement and temperature control are employed. The flow field is visualized from the side of the cell by a shadowgraph optical method. The experiment and data acquisition are controlled by an 80286 microcomputer, and data analysis and image processing are done on the microcomputer and on a MIPS workstation.

3.1 Convection cell

The convection cell used in our experiments is a rectangular cell with a height $h = 0.462$ cm, which is larger than the width $b = 0.140$ cm, but much smaller than the length $L = 6.383$ cm. The aspect ratio $\frac{L}{h} : \frac{b}{h} : 1$ is 13.8 : 0.3 : 1. The cell, which is machined from aluminum plate, is shown in Figure 3.1. About 1 cm above and below the cell the aluminum widens to 1.27 cm. The bottom plate of the cell is heated by an electric foil heater with resistance 71.1Ω [31], and the top plate is in good thermal contact with continuously circulating, temperature regulated water. Two calibrated thermistors are embedded in holes in the top and bottom plates (A and B in figure 3.1) for measurement of the temperatures. The transparent side walls of the cell are made out of glass microscope slides 0.96 mm thick with good optical quality, glued to the aluminum with silicone sealant. The thermal conductivity of the glass is on the order of $0.8\frac{W}{mK}$ [32], comparable to that of the ethanol-water mixtures. The heat conducted through the side walls is estimated to be $2 \sim 3$ times that conducted through the cell (sample fluid). The cell is filled with the experimental fluid through two stainless-steel capillaries which are epoxied into holes at the left and right ends of the cell. The left and right end walls of the cell are made very narrow to minimize heat transfer through the aluminum. Two small "ears" were machined at the left and right top corners for the purpose of trapping possible air bubbles.

The sample cell hangs at the center of a copper cylinder of diameter 10.5 cm, which is in thermal contact with the circulating cooling water. The copper cylinder sits on a levelling plate and is surrounded by insulating foam contained in a cubic wooden box of side 40 cm. This box is itself surrounded by styrofoam

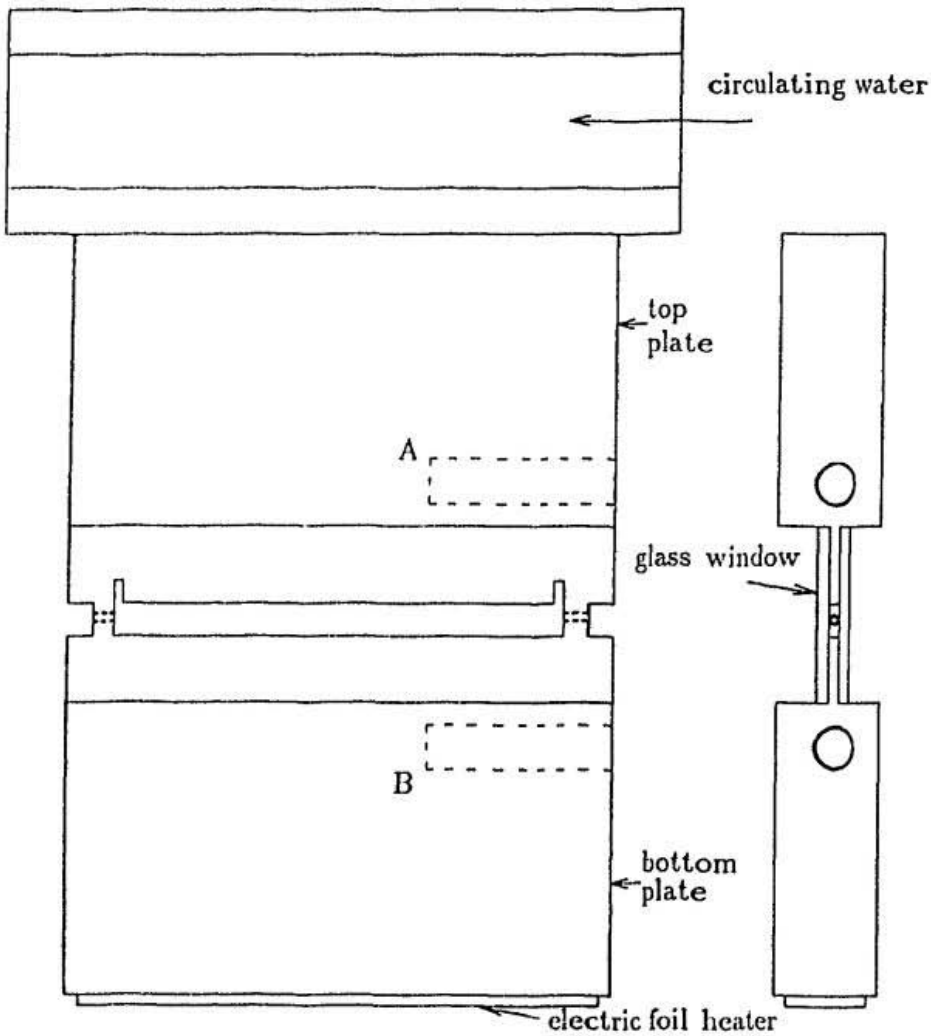

Figure 3.1: Sketch of the convection cell.

insulation.

3.2 Temperature control

Accurate temperature control is a requirement for our experiment. Shown in Figure 3.2 is a sketch of our temperature control system. The temperatures of the top and bottom plates of the convection cell are detected by two calibrated thermistors at holes A and B of Figure 3.1. The thermistor resistances are monitored with $6\frac{1}{2}$-digit digital multimeters (Keithley Model 196) and transmitted by an IEEE-488 bus to a microcomputer.

The temperature of the top plate is controlled by the circulating water, which is in good thermal contact with the top plate. In our experiment, the top plate is maintained at $18.000 \pm 0.001°C$. The circulating water is pumped by a temperature controlled water bath (Lauda Refrigerating Circulators Model RMS-6), which has a control accuracy of $\pm 0.01°C$. This circulating water is further temperature regulated using a heater consisting of a length of wire past which the water flows. The microcomputer, after comparing the temperature read in by the thermistor with the pre-set temperature, sends out a voltage signal through a D/A converter (Lab Master DMA). This voltage is then amplified by a DC amplifier (Kepco Model BOP 20-10M) and applied to the heater.

Before each run of our experiment, the temperature difference ΔT between the top and bottom plates has to be set. This temperature difference is controlled to an accuracy of $\pm 0.002°C$ in our experiment by regulating the voltage applied to the bottom heater while the top plate temperature is regulated independently. The computer reads in the temperatures of the top and bottom

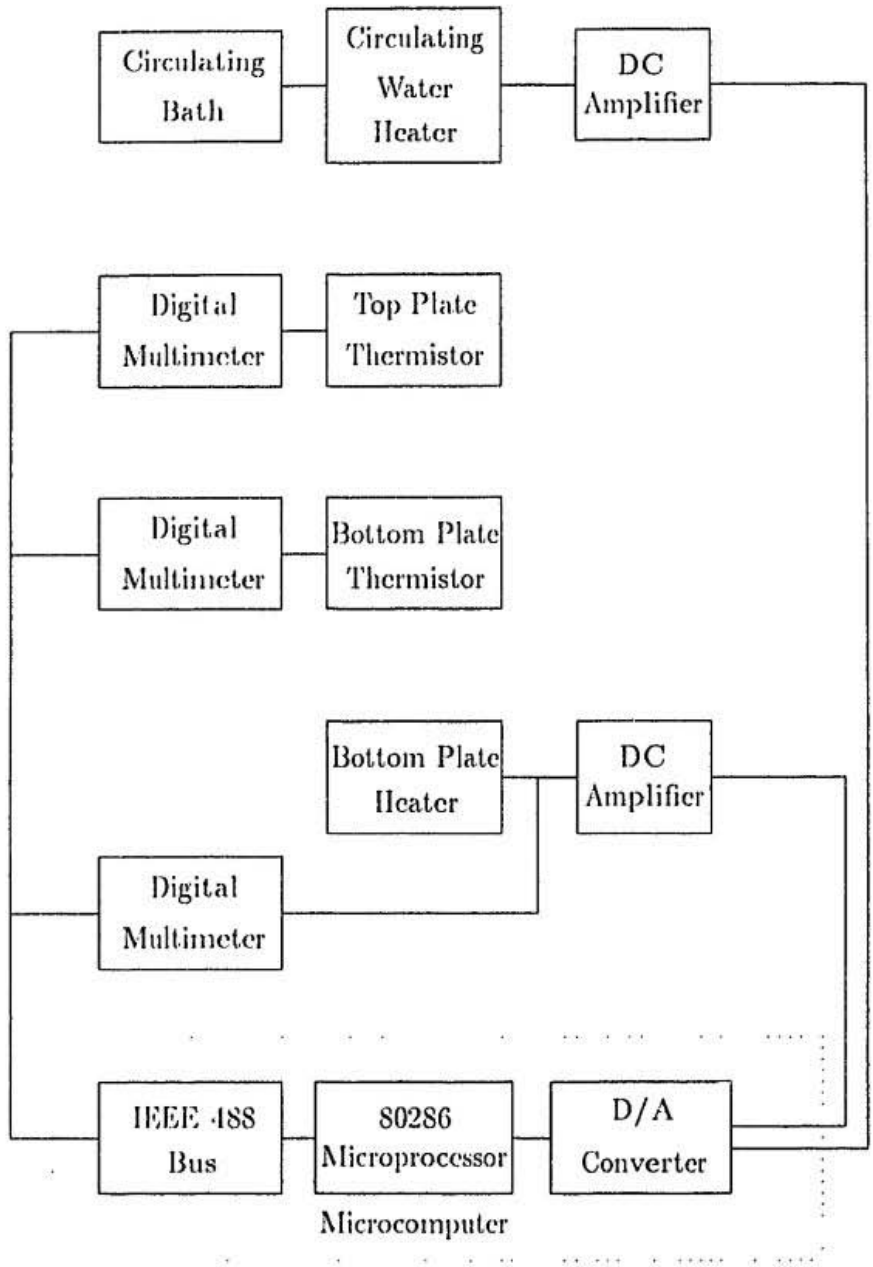

Figure 3.2: Temperature control system

plates, compares their difference with the pre-set value of ΔT and then sends out a voltage signal through a D/A converter. After being amplified by a second DC amplifier, this voltage is applied to the bottom heater to regulate the temperature difference.

During a run of the experiment, the temperature of the bottom plate, and thus the temperature difference, is no longer controlled by regulating the voltage supplied to the bottom plate heater. Instead, the power (or equivalently, the voltage) supplied to the bottom plate heater is fixed for each step of a run. In this case, the measured temperature difference is found to be stable within $\pm 0.005°C$.

The voltage applied to the bottom heater for each step of a run is also monitored by a $6\frac{1}{2}$-digit digital multimeter and transmitted by the IEEE 488 bus to the microcomputer. This voltage is used to calculate the Nusselt number.

3.3 Shadowgraph flow visualization

We use shadowgraph flow visualization to view the convecting flow due to the applied temperature gradient and induced concentration gradient. The optical arrangement is shown schematically in Figure 3.3. The light source is an AND Kilobright red light emitting diode (LED), the front surface of which is machined close to the diode junction and polished smooth. Light from the LED is passed through a spatial filter with a 50 μm pinhole to approximate a point light source. A collimating lens is used to produce a parallel light beam which is sent through the convection cell. The shadowgraph intensity profile of the convection flow pattern is then obtained by a CCD camera.

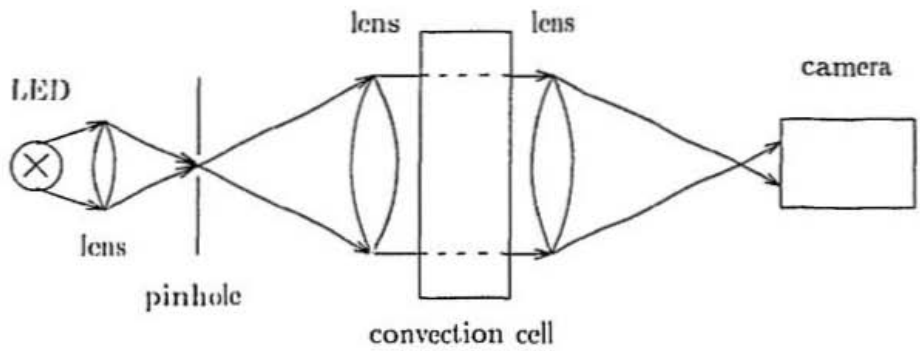

Figure 3.3: Shadowgraph system with parallel light through the convection cell.

The principle of the shadowgraph method is shown in Figure 3.4 [33]-[35]. The parallel light is deflected as it passes through the convection cell because the refractive index varies with position in the convecting fluid. The rising fluid is warmer and less dense, and thus has a smaller refractive index than the descending fluid, which is cooler and more dense. The light is refracted and focussed towards the regimes that correspond to the descending fluid. Concentration gradients also alter the fluid density and the refractive index. Therefore, the shadowgraph intensity recorded by the camera yields information about the temperature and concentration field of the flow.

It can be shown that the intensity I of the shadowgraph image is given by [33]

$$I = k\nabla_h^2 n \tag{3.1}$$

where k is a constant, n is the refractive index, and $\nabla_h^2 = \partial^2/\partial x^2 + \partial^2/\partial z^2$ is the two dimensional Laplacian. Here x is the coordinate along the long dimension

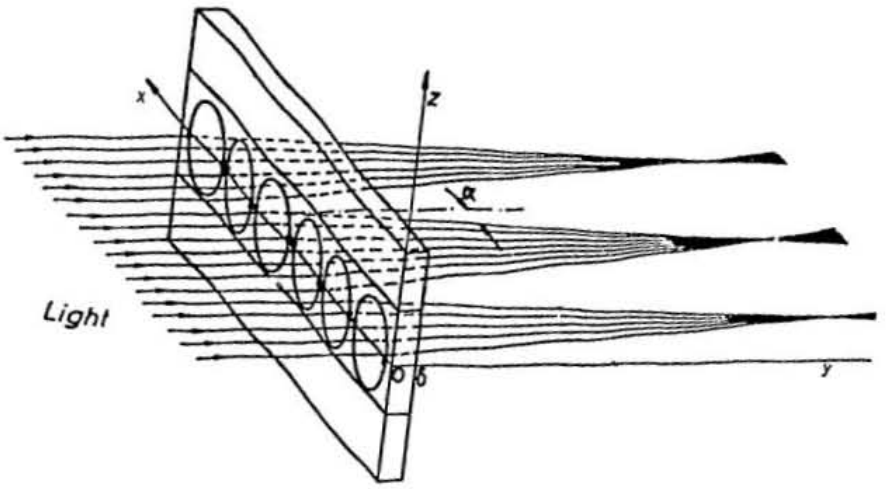

Figure 3.4: Principle of the shadowgraph method: The incoming parallel light is deflected according to the gradient of the refractive index.

of the cell, and z the vertical coordinate. Light enters the cell traveling in the y direction, and fluid properties are assumed to be constant along the y direction. For thermal convection of binary fluids, the refractive index changes with temperature T and concentration c, and for small variations of T and c about their mean values T_0 and c_0, we can write

$$n = n_0 + \left.\frac{\partial n}{\partial T}\right|_c (T - T_0) + \left.\frac{\partial n}{\partial c}\right|_T (c - c_0) \tag{3.2}$$

where $n_0 = n(T_0, c_0)$. Assuming $\left.\frac{\partial n}{\partial c}\right|_T$ and $\left.\frac{\partial n}{\partial T}\right|_c$ to be constant at given c and T, eq. (3.1) can be written as

$$I(x, z) = A(\nabla_h^2 c + b\nabla_h^2 T) \tag{3.3}$$

or

$$I(x, z) = A\left[\left(\frac{\partial^2}{\partial x^2} + \frac{\partial^2}{\partial z^2}\right)c(x, z) + b\left(\frac{\partial^2}{\partial x^2} + \frac{\partial^2}{\partial z^2}\right)T(x, z)\right] \tag{3.4}$$

where $A = k\left.\frac{\partial n}{\partial c}\right|_T$ and $b = \left.\frac{\partial n}{\partial T}\right|_c \Big/ \left.\frac{\partial n}{\partial c}\right|_T$ are constants at given T and c. We can see that b measures the relative importance of the contribution to the shadowgraph intensity due to variations of the concentration field to that due to variations of the temperature field. Eq. (3.4) will be applied when comparing our experimental data with the numerical results. Because dimensionless equations were used in the numerical calculations [13, 14], we have to non-dimensionalize b as

$$b = \frac{\beta}{\alpha}\frac{\partial n/\partial T|_c}{\partial n/\partial c|_T} \tag{3.5}$$

where α is the thermal expansion coefficient and β the solutal expansion coefficient.

3.4 General procedure

The sample fluid used in our experiment is a solution of 25% by weight ethanol in water. Some properties of ethanol-water solutions are given in the Appendix. At the mean temperature of 22.84°C, we estimate, using the fluid properties given in the Appendix and in ref. [36], a mean separation ratio $\psi \simeq -0.08$, a Lewis number of 0.01, and a Prandtl number of 19. The estimated separation ratio and Lewis number are the same as those used in the numerical calculations [14, 18]. The vertical thermal diffusion time is $\tau_v = d^2/\kappa \simeq 200s$ and vertical mass diffusion time $\tau_m = d^2/D_m \simeq 22000s$.

The temperature at the top plate is always maintained constant at 18°C. Before a run, the temperature difference between the top and bottom plates is set at a value within the conduction state of the fluid but close to the onset of convection and held there for two days, long enough for the establishment of the temperature induced concentration gradient due to the Soret effect to occur. By using eq. (2.46) and the Soret coefficient from Ref. [36], the induced concentration difference Δc between the top and bottom plates is estimated to be $\sim 0.3\%$ at the mean temperature of 22.84°C and the temperature difference ΔT of 8.9°C, which is just below the onset. This Δc is much smaller than the mean concentration of 25%, thus does not affect the fluid properties substantially. We begin a run by incrementing the heat current Q applied to the bottom plate in steps of $\sim 1\%$ through its critical value Q_c. Between each step, we wait for times of approximately 100 τ_v.

Shadowgraph images are taken by a CCD camera (Burle TC100) which is controlled by the microcomputer through a PC Eye interface board. A

monitor (Burle TC1910A) is used to display the shadowgraph images from the camera through the PC Eye interface board. The video camera has a nonlinear response at weak and strong light intensities, so it was calibrated against a photodiode with a linear response to light intensity. Calibration was done with the fluid in the conductive state. The shadowgraph intensity taken by the camera is averaged over all points within the flow field (500×30 pixels). The corresponding light intensity is given by the photodiode, which monitors the same light source via a beam splitter. Based on these measurements at different light intensities, a calibration curve for the camera is obtained.

To minimize the effects of nonuniform illumination across the cell, imperfections in the optics, *etc.*, and to increase the sensitivity of the shadowgraph to the small changes in refractive index that accompany the onset of convective flow, we also take a background shadowgraph image in the conduction state of the fluid and divide all subsequent shadowgraph images by this background image.

For each step of a run, we read the temperature difference between the top and bottom plates and the power supplied to the bottom plate. From these measurements and the known properties of the fluid mixture, the Rayleigh and Nusselt numbers can be calculated. We also take three types of shadowgraph images. One is a shadowgraph of the entire flow field from which we get a two-dimensional shadowgraph intensity distribution. The second is a "space-time" image which is made up of a series of shadowgraphs taken at the middle horizontal line of the cell every $1.5\tau_v$. The third one is the time series of the shadowgraph intensity at the middle point of the cell (averaging 2×2 pixels), for which the intensity was recorded every $0.15\tau_v$.

Chapter 4

Experimental Results and Analysis

In this Chapter, our experimental results from runs with a 25% by weight ethanol-water mixture, with a top plate temperature of 18°C are presented and discussed. Over a run, the temperature difference between the top and bottom plates varies typically from 8.5°C to 10.5°C. The bifurcation properties at the onset of convection and at the second transition from TW state to stationary overturning convection state are discussed first. Then we present measurements of the shadowgraph intensity profile, and discuss the effect of the concentration field on the shadowgraph signals observed in both TW and SOC states.

We also did several runs of our experiment for 25% ethanol-water mixtures with a top plate temperature of 26°C, and for 8% ethanol-water mixtures at various top plate temperatures. We did not get usable results in these runs. For the 8% mixture, we did not even observe TWs, despite the fact that

the range of r over which the TW state exists is expected to be larger for the 8% mixture than for the 25% mixture [14]. These results might indicate that the strongly one-dimensional geometry used in our experiment has a very significant effect on the dynamics of the system. In addition, the properties of our sample likely deviate significantly from the Boussinesq approximation, and this may also have an effect. There are other possible explanations, however. It may be that some unknown feature of our cell pins the traveling waves and prevents them from propagating. It is also possible that our samples become contaminated somehow, since sometimes (but not always) the results were not repeatable.

The results presented here for the 25% ethanol-water mixture come from the only set of runs that showed TW behaviour consistently from one run to the next.

4.1 Bifurcation properties

Convection is observed to begin at $\Delta T_c = 8.91°C \pm 0.01°C$, with a backward bifurcation from the conduction state to a stable nonlinear TW state. The corresponding critical Rayleigh number at the onset is $r_c = R_c/R_0 = 1.34 \pm 0.01$, where R_0 is the critical Rayleigh number for the onset of the convection with pure water in the same cell. The average temperature in the cell at the onset of convection is $22.81°C \pm 0.01°C$. From the fluid properties given in the Appendix, the separation ratio is estimated [36] to be $\psi = -0.08$. As r is increased to $r^* = 1.43$, a second transition from TW to SOC is observed.

Shown in Figure 4.1 is the Nusselt number $N - 1$ as a function of Rayleigh number r. As mentioned in Chapter 1, N is a convenient quantity for the

characterization of convective flow, and is defined as the ratio of the total heat flux through the convecting layer to that due to thermal conductance. Since the heat supplied to the bottom plate is transported to the top plate through the side and end walls of the cell as well as through the sample, we have to calculate and subtract the heat flux through the cell (which is assumed to be constant), when calculating N. To do this, we did a straight line fit to measurements of ΔT as a function of the power supplied to the bottom heater in the conduction state. This gives the effective thermal conductance of the cell and sample. Then the constant effective thermal conductance of the cell is calculated by subtracting the known thermal conductance of the sample. Subtracting this effective thermal conductance due to the cell from the total effective thermal conductance (in both conduction and convection states) gives the effective thermal conductance due to the sample only. Finally, N is calculated by dividing this quantity by the known thermal conductance of the sample.

As seen in Figure 4.1, the Nusselt number is about 1 in the conduction state, as it should be. At r_c, there is a discontinuous transition from the conduction state to a convection state. Because convective flow enhances the heat transfer through the layer, and because the amount of heat supplied to the bottom plate is fixed, the temperature difference across the layer decreases when convection sets in, corresponding to a decrease in Rayleigh number. If the Rayleigh number is increased further above the onset, the Nusselt number also increases slightly, indicating that the convection amplitude becomes larger and thus more heat is transferred.

Figure 4.2 shows typical shadowgraph images taken at a series of different Rayleigh numbers. All shadowgraph images have been divided by the back-

ground image. The bright regions in the image correspond to cold falling fluid while the dark regions correspond to warm rising fluid. Between r_c and r^*, when the system is in the TW state, the convection rolls are found to be moving, while in the SOC state when $r > r^*$, they are fixed in space. This motion is shown more clearly in the "space-time" shadowgraph images (Figure 4.3) taken at the middle line of the cell every 300 seconds. For each Rayleigh number, ten lines are shown in Figure 4.3. Close to the onset, the convection rolls move to the left relatively quickly. As r is increased, they slow down, and finally stop moving at $r = r^*$. Some of the TW characteristics in Figure 4.3 appear to be non-uniform, mainly due to the way that the images were sampled. It is also interesting to notice that the TW direction is reversed when r approaches r^*. This reversal, which we are unable to explain, does not exist in the numerical calculations of Ref. [14] and in the measurements of Ref. [16].

Plotted in Figure 4.4 is the TW frequency ω as a function of Rayleigh number. The TW frequency is obtained from the shadowgraph intensity profile taken at a fixed point in the cell while the TW passes by it. The time t between adjacent maxima in the optical intensity is averaged and scaled by $\tau_v = d^2/\kappa$ to give a dimensionless time, τ. The dimensionless TW frequency is then given by $\omega = 2\pi/\tau$. This frequency is found to decrease monotonically as r is increased, dropping most quickly near the onset of the convection, in general agreement with theoretical [12] and numerical results [13], as well as with other experimental measurements [11, 15, 16].

In a laterally infinite system with $\psi = -0.08$, numerical calculations [14] predict the onset of convection to occur at $r_c = 1.0965$ with a dimensionless TW frequency $\omega = 5.753$ while the transition from TW to SOC occurs at $r^* \simeq 1.09$, which is smaller than r_c. This implies that TW would only be seen

when r is decreased below r_c after the onset of convection. The calculations of Ref. [14] also predict that TW will exist over a range of r of only about 0.3. In contrast, we observed TWs over a range of r about three times as large, extending to well above the onset. The measured TW frequency at the onset is 6.01, somewhat larger than the calculated value for the Hopf frequency for a laterally infinite system. Ohlsen *et al.*[16] observed the same behaviour in their cell for $\psi = -0.25$, and pointed out that this is apparently generally the case, although no predictions of the effect of cell width on ω_H have been made. Our TW frequency decreases much more rapidly just above onset than did the measurements of Ref. [16]. This difference is in qualitative agreement with the behaviour calculated in Ref. [14] for mixtures with $\psi = -0.25$ and -0.08. After the initial rapid drop, ω remains almost constant until going to zero at the transition to SOC; in the calculations [14] this region does not occur. Our measurements did not extend close enough to the TW-SOC transition to permit us to make any comment on the nature of the transition, or on the behaviour of ω there.

4.2 Structure of TW and SOC states

We studied the role of the concentration field in the dynamics of the TW and SOC states by comparing our experimental shadowgraph intensity profiles with the numerically calculated ones [18]. Presented first in this section are the numerical results, which were calculated with fluid parameters $\psi = -0.08$, $\sigma = 10$ and $L = 0.01$. We "analyze" the numerical results in two ways: by averaging them over the vertical dimension z to get an integrated shadowgraph intensity [17] and as a function of z. The experimental results are then studied

in the same way.

Shown in Figure 4.5 are the vertical averages of numerically calculated temperature field $\overline{\theta}(x)$, concentration field $\overline{c}(x)$, their second derivatives $\frac{\partial^2\overline{\theta}}{\partial x^2}$ and $\frac{\partial^2\overline{c}}{\partial x^2}$, and the calculated shadowgraph signal $I(x)$ for TW at two Rayleigh numbers ($r_1 = 1.0635$, $r_2 = 1.074$). After averaging over z, we interpolated between the calculated data points for $\overline{\theta}(x)$ and $\overline{c}(x)$ using a polynomial interpolation routine [38]. The second derivatives are calculated from the original $\theta(x,z)$ and $c(x,z)$, then averaged over z and interpolated. $I(x)$ is calculated from $\frac{\partial^2\overline{\theta}}{\partial x^2}$ and $\frac{\partial^2\overline{c}}{\partial x^2}$ using eq. (3.4) with $A = 1$ and $b = -0.908$, where b is calculated for the mean cell temperature of 22.84°C. As indicated by Figure 4.5(c), in a TW there is a difference in the concentration between adjacent rolls with opposite vorticity, while the concentration within a roll is approximately constant. Thus, the concentration is uniform, except in the regions of strong upflow and downflow at the roll boundaries, and in the boundary layers near the top and bottom plates. The concentration difference between rolls becomes smaller as r is increased, and decreases to zero when $r > r^*$. The width of each boundary layer near the top and bottom plates and between the rolls shrinks as r is increased, albeit not to zero. At the transition from TW to SOC at r^*, the mirror-symmetry between left-turning and right-turning rolls is restored. Thereafter, the concentration field is almost laterally homogeneous, except for a mirror-symmetric variation at the upflow and downflow regions at the roll boundaries. The maxima of $I(x)$ correspond to the downflow and the minima to the upflow. In the TW state, there is a phase difference between the main peaks in $\frac{\partial^2\overline{c}}{\partial x^2}$ and the extrema of $\frac{\partial^2\overline{\theta}}{\partial x^2}$. This phase difference, and the corresponding one between the temperature and vertical velocity, vanish at the TW to SOC transition. The calculated temperature and concentration

fields in the SOC and TW states are both symmetric under lateral translation by $a/2$, where a is the wavelength of a roll pair, and subsequent reflection at the horizontal midplane of the fluid layer, but the mirror symmetry between left-turning and right-turning rolls is broken in a TW. Thus the optical signal calculated for the TW state shows the symmetry $I(x + a/2) = -I(x)$, but not the mirror symmetry around upflow and downflow boundaries that characterizes a SOC state.

We can easily distinguish the contribution due to the concentration from that due to temperature. The temperature contribution to $I(x)$ is smooth, nearly sinusoidal, and almost symmetric about the upflow and downflow boundaries, whereas the concentration contribution has sharp maxima and minima as well as two side peaks associated with each of these features, which become bigger if r is increased.

Shown in Figure 4.6 are calculated optical signals at various vertical positions z for TW states at $r_1 = 1.0635$ and $r_2 = 1.074$. The optical signal around the middle line of the fluid layer looks almost the same as the vertically averaged signal. Close to the top plate, the sharp feature at the minimum becomes smaller and the optical intensity varies more smoothly around the minimum. This indicates that the contribution from the concentration around the optical minimum (warm rising flow) is smaller near the top plate. Similarly, close to the bottom plate the sharp feature at the maximum of optical signal shrinks, indicating a smaller contribution from the concentration field around the maximum (cold falling flow).

Our experimental shadowgraph data, taken with the video camera, are first corrected for the nonlinear response of the camera, then divided by the background image. The resulting intensity profile is smoothed to remove high

frequency noise. The smoothing involves an FFT procedure with a spatial filter which cuts off the high frequency components [38]. The smoothing used corresponds roughly to removing variations with a wavelength smaller than three pixels.

Shown in Figure 4.7(a) is the vertically averaged experimental shadowgraph intensity in an SOC state with $r = 1.54$. Figure 4.7(b) shows the vertically averaged shadowgraph intensity for a convection state for pure water (in the same cell) at $r = 1.19$. By comparing these two figures, we can see that without the contribution of the concentration field, the shadowgraph intensity in the pure water case is quite smooth and almost sinusoidal. In the mixture, on the other hand, the shadowgraph intensity has sharp features. This clearly illustrates that it is the concentration field that contributes the sharp features to the shadowgraph profile of Figure 4.7(b).

Shown in Figure 4.8 is the measured shadowgraph intensity, averaged over the height of the cell, for TW states moving to the left and for SOC states. The main peaks are found to be higher and wider relative to the smooth background than predicted by the numerical calculations. Only one side peak is observed between the maxima and minima, while the numerical results predicted two side peaks between the maxima and minima. Since measurements of the intensity at a single fixed point in the cell as the TW propagates past that point do show two side peaks, this difference is most likely due to limitations in the resolution of our optical system. The intensities of the main peaks as well as of the side peaks increase as the Rayleigh number is increased. This indicates that the contribution to the optical signal due to $\frac{\partial^2 \overline{c}}{\partial x^2}$ becomes larger when r is increased, as also found in the numerical results shown in Figure 4.5. The absence of mirror symmetry between adjacent rolls and the phase shifting

predicted for the TW states are not easily seen.

Shown in Figure 4.9 is the shadowgraph intensity for a TW state with $r = 1.29$ at several vertical positions in the cell. The signals are noisier than the vertically averaged ones shown in the previous figure, which used the same smoothing cut off frequency. The maxima and the minima have approximately the same intensity at $z = 0.44$ while in the numerical results the maxima and minima are the same size at the middle of the cell, $z = 0.5$. For $z > 0.44$, toward the top of the cell, the minima of the shadowgraph intensity decrease quickly in strength and become indistinguishable from the experimental noise. Similarly, moving toward the bottom of the cell, the maxima quickly become smaller. The decrease of the maxima or minima when close to the bottom or top of the cell is in qualitative agreement with the numerical prediction, as shown in Figure 4.6, but they shrink much faster than predicted. Again, we are unable to say whether this is a real effect due to our one-dimensional cell, or whether it is due to residual nonlinearity in the camera response.

Less noisy intensity profiles can be obtained by recording the optical signal at a fixed point in the cell while TW patterns propagate past this point. Figure 4.10 shows intensity profiles taken at the middle point of the cell for TWs moving to the left at various Rayleigh numbers. The maxima do not have the same size as the minima in these intensity profiles. As described above, the measured maxima and minima were found to be approximately the same size slightly below $z = 0.5$. The intensity profiles presented in this figure are at the same z value as that in Figure 4.9(b). It can be seen that the two side peaks between the maxima and minima are now distinguishable. The left side peak of the main peak – on the side towards which the rolls are traveling is higher than the right side peak, as also seen in numerical prediction for

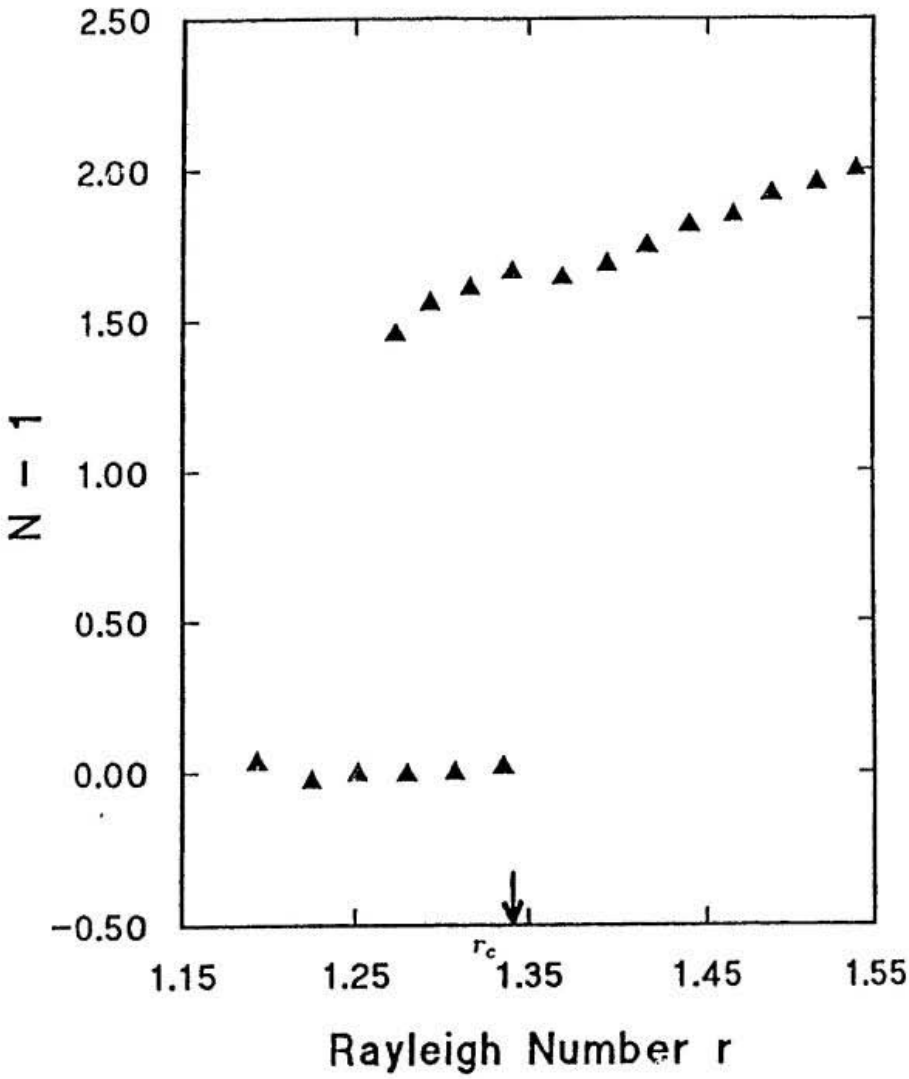

Figure 4.1: Nusselt number $N - 1$ as a function of Rayleigh number r.

TWs. No systematic phase shifts between main peaks at different Rayleigh numbers are observed within our experimental limitations except for the TW state at $r = 1.38$ (close to r^*), which has an obviously non-symmetric intensity profile and a large phase shift of the main peaks compared with those at lower Rayleigh numbers. This is not expected from the numerical predictions for laterally infinite systems. We speculate that this might again be due to the narrow geometry we used in our experiment.

By comparing our experimental results with numerical predictions, we do see the sharp features in the shadowgraph intensity profile contributed by the concentration field, for both TW states and SOC states. We are, however, unable to confirm many of the detailed predictions of the numerical results, including that of the breaking of mirror symmetry in the TW states, at least partly due to the limitations of our shadowgraph optical system.

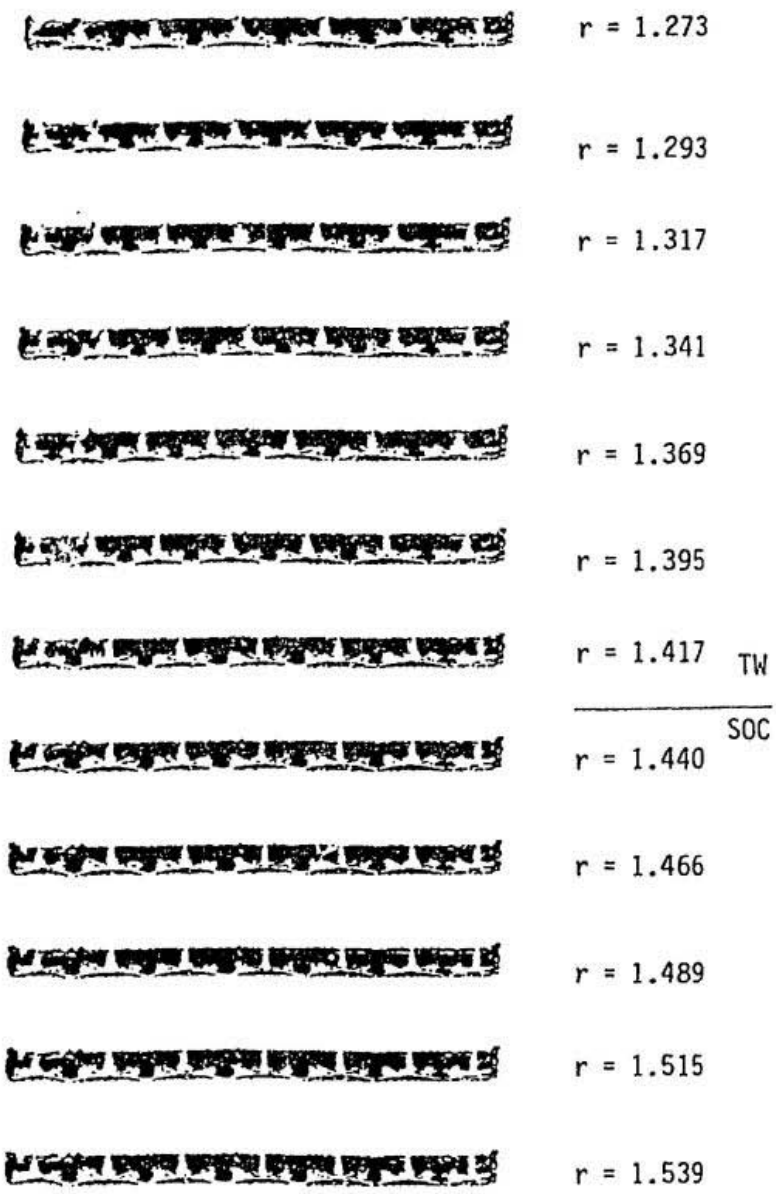

Figure 4.2: (a) Typical shadowgraph images at various Rayleigh numbers, showing TWs moving to the left and SOC states.

Figure 4.2: (b) A shadowgraph image of a TW convection state at $r = 1.37$. Light regions correspond to downflow and dark regions to upflow. The convection pattern in this case consists of 13 rolls traveling to the left.

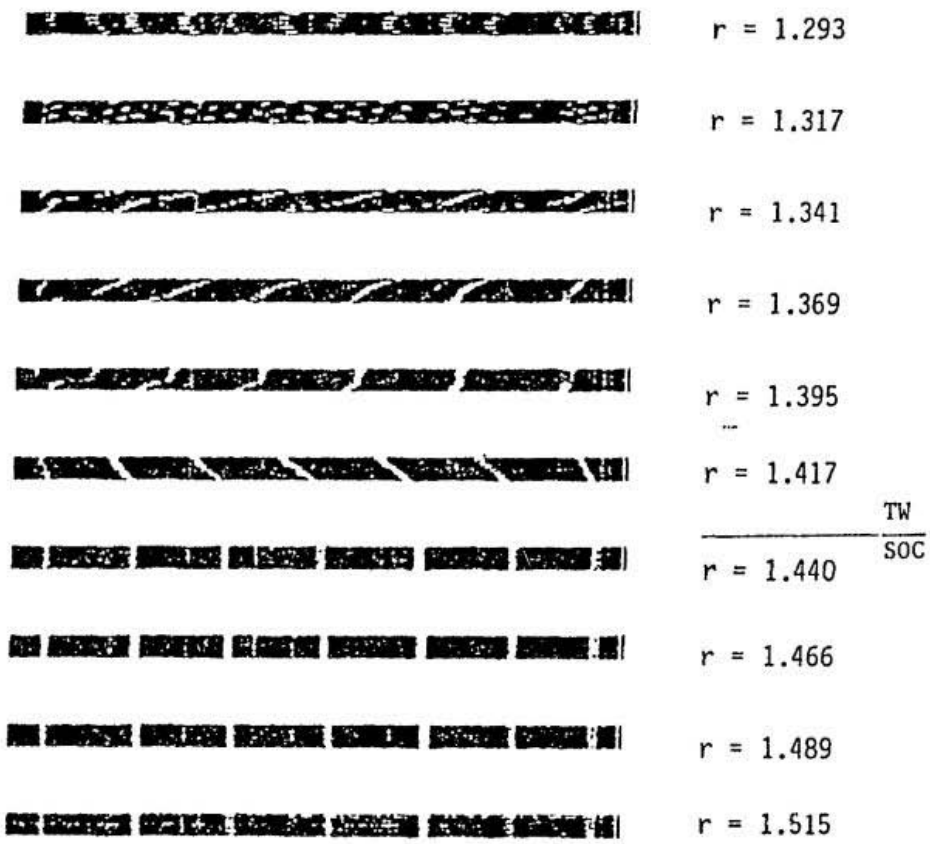

Figure 4.3: Shadowgraph "space-time" images at various Rayleigh numbers, illustrating travelling wave convection over a range of r.

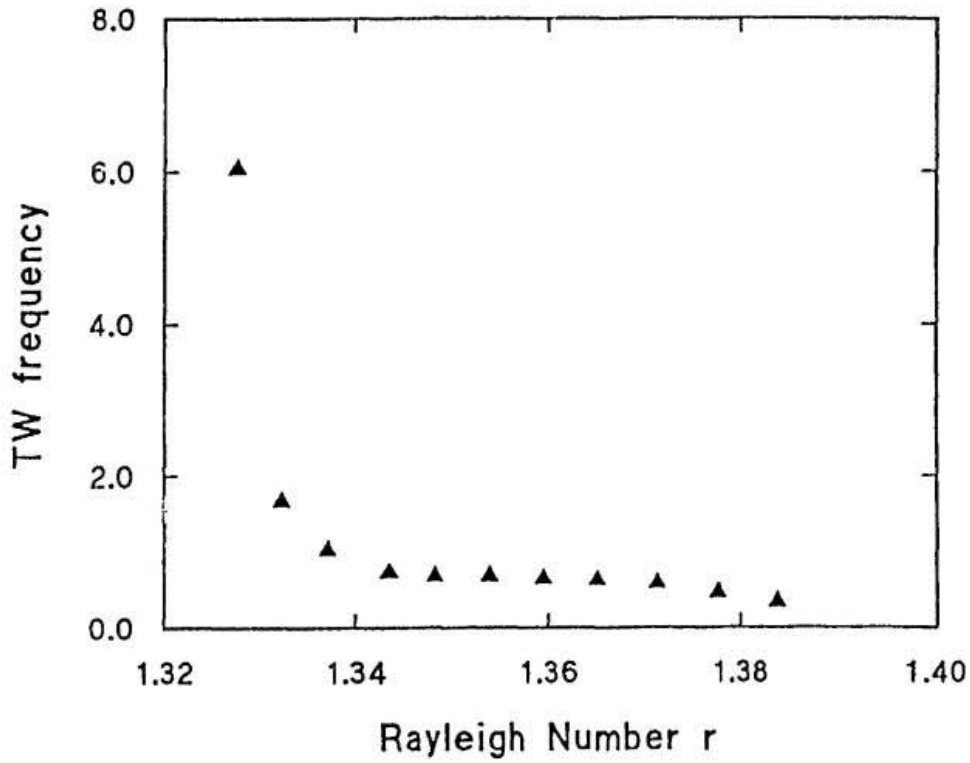

Figure 4.4: Traveling wave frequency ω as a function of Rayleigh number.

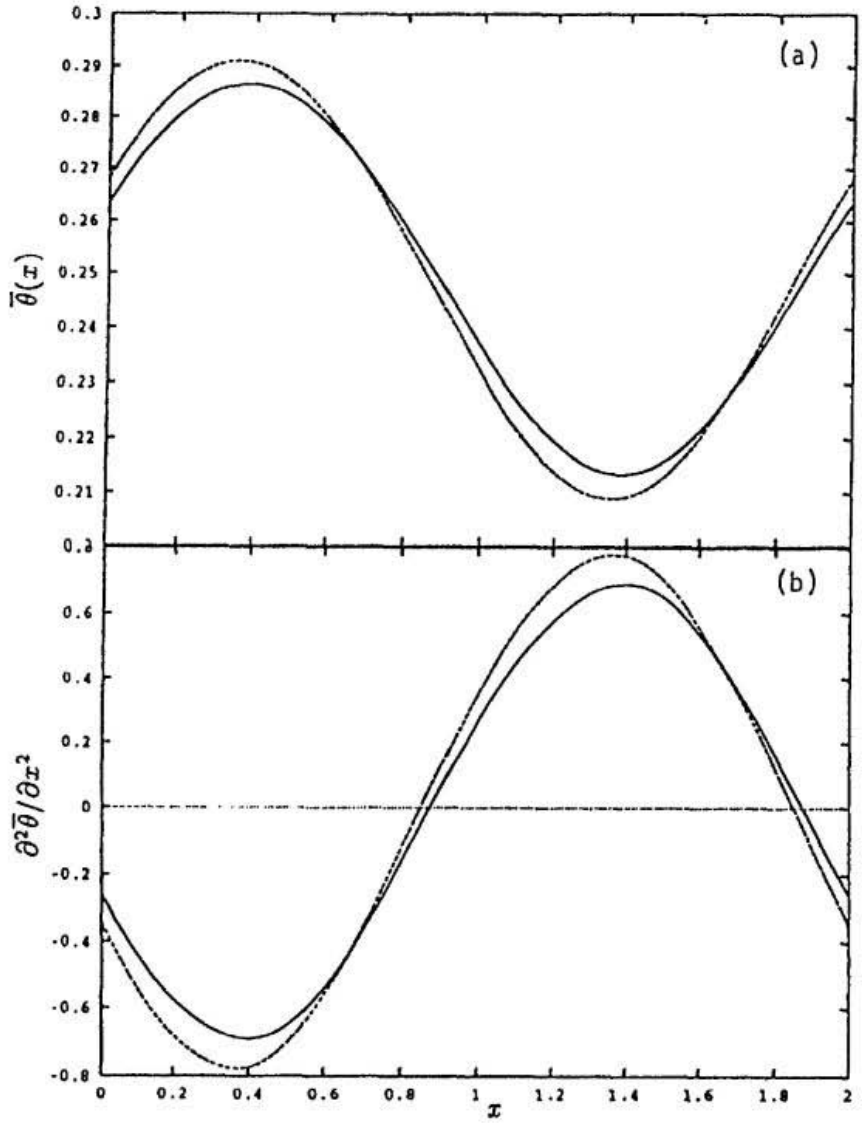

Figure 4.5: Numerical results for the vertically averaged temperature field $\overline{\theta}(x)$, concentration field $\overline{c}(x)$, their second derivatives $\partial^2\overline{\theta}/\partial x^2$ and $\partial^2\overline{c}/\partial x^2$, and the calculated optical profile $I(x)$. Shown are right-moving TWs with $r_1 = 1.0636$ (solid line) and $r_2 = 1.074$ (dashed line). (a) $\overline{\theta}(x)$, (b) $\partial^2\overline{\theta}/\partial x^2$, (c) $\overline{c}(x)$, (d) $\partial^2\overline{c}/\partial x^2$, and (e) $I(x)$, all in arbitrary units. x is the horizontal dimension in the unit of half a wavelength, $a/2$. Numerical data for (a)-(d) were originally from [18] and were averaged and smoothed before plotting.

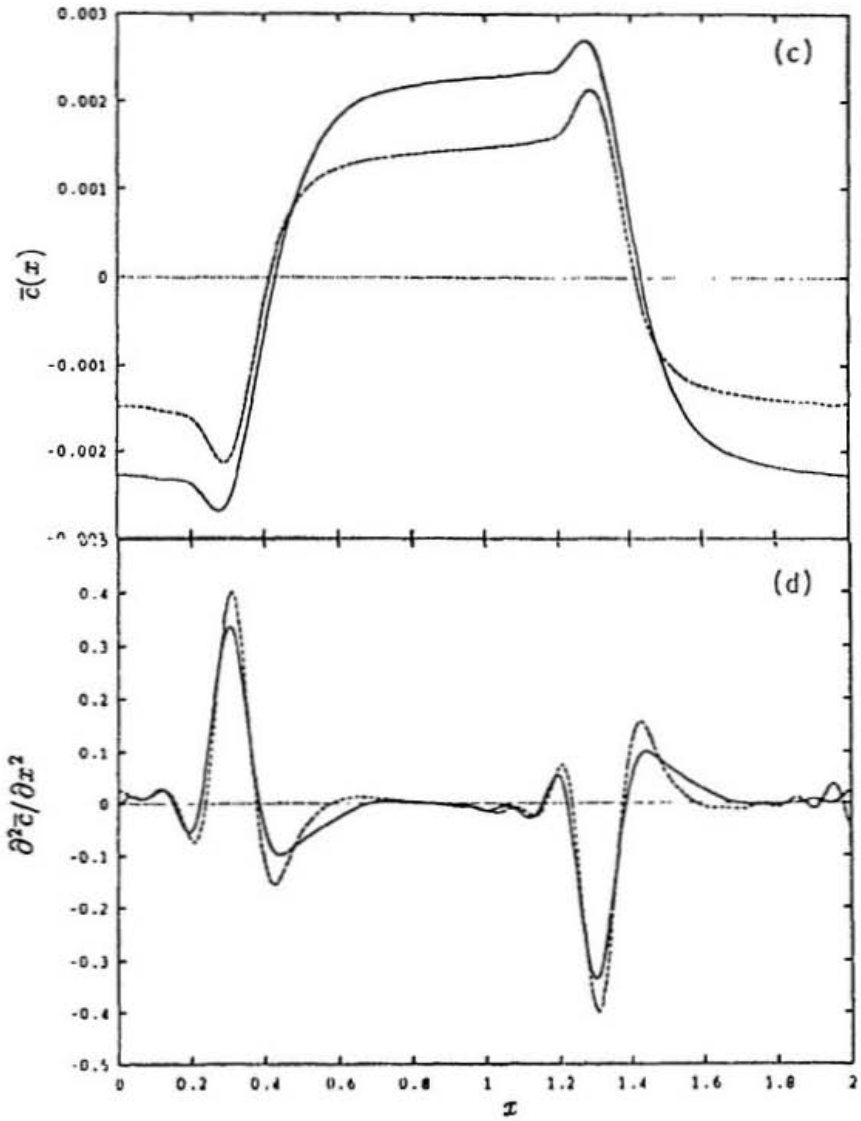

Figure 4.5: (continued).

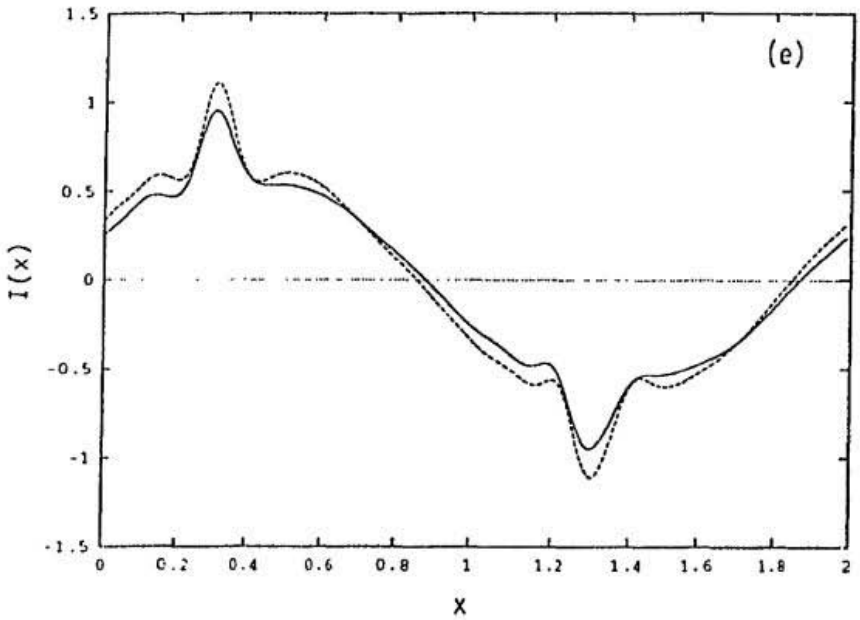

Figure 4.5: (continued).

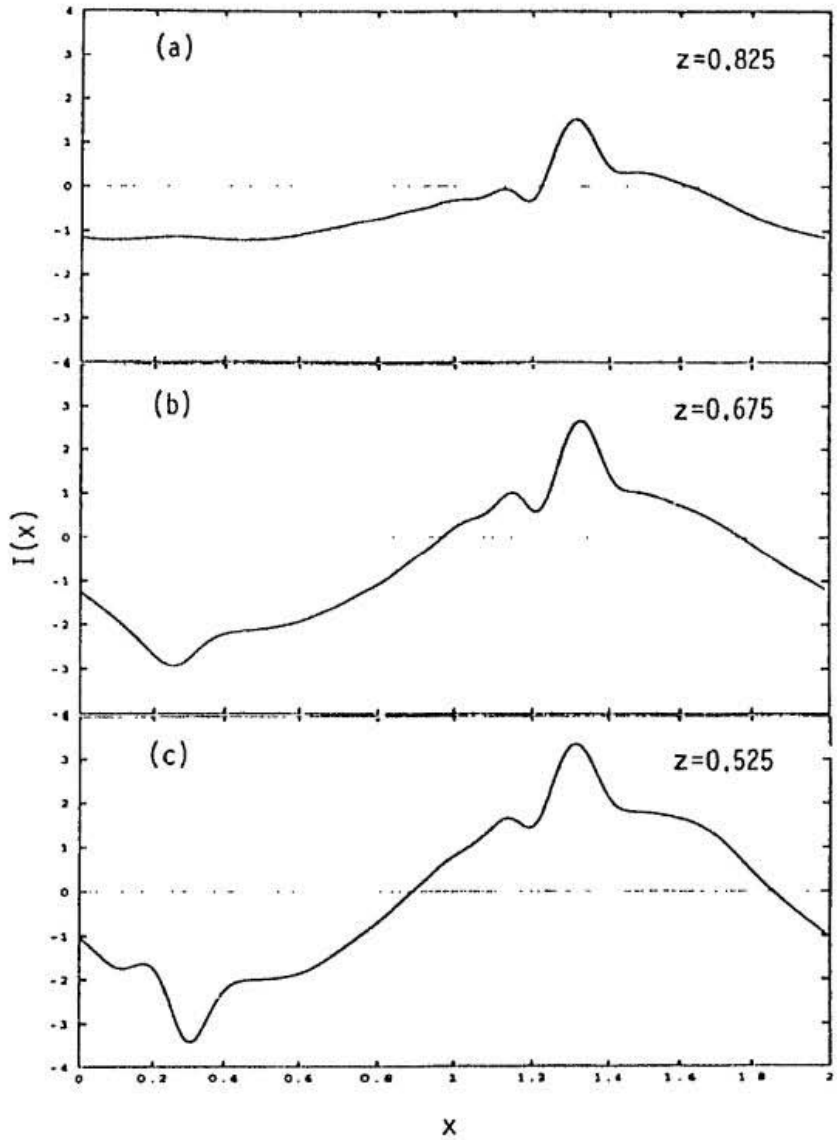

Figure 4.6: Numerically calculated shadowgraph intensities at various vertical positions z of the cell for TWs moving to the right at (a)-(f) $r_1 = 1.0635$ and (g)-(l) $r_2 = 1.074$. I is in arbitrary units, x in units of $a/2$ and z in units of d. I was calculated from θ, c data from [18].

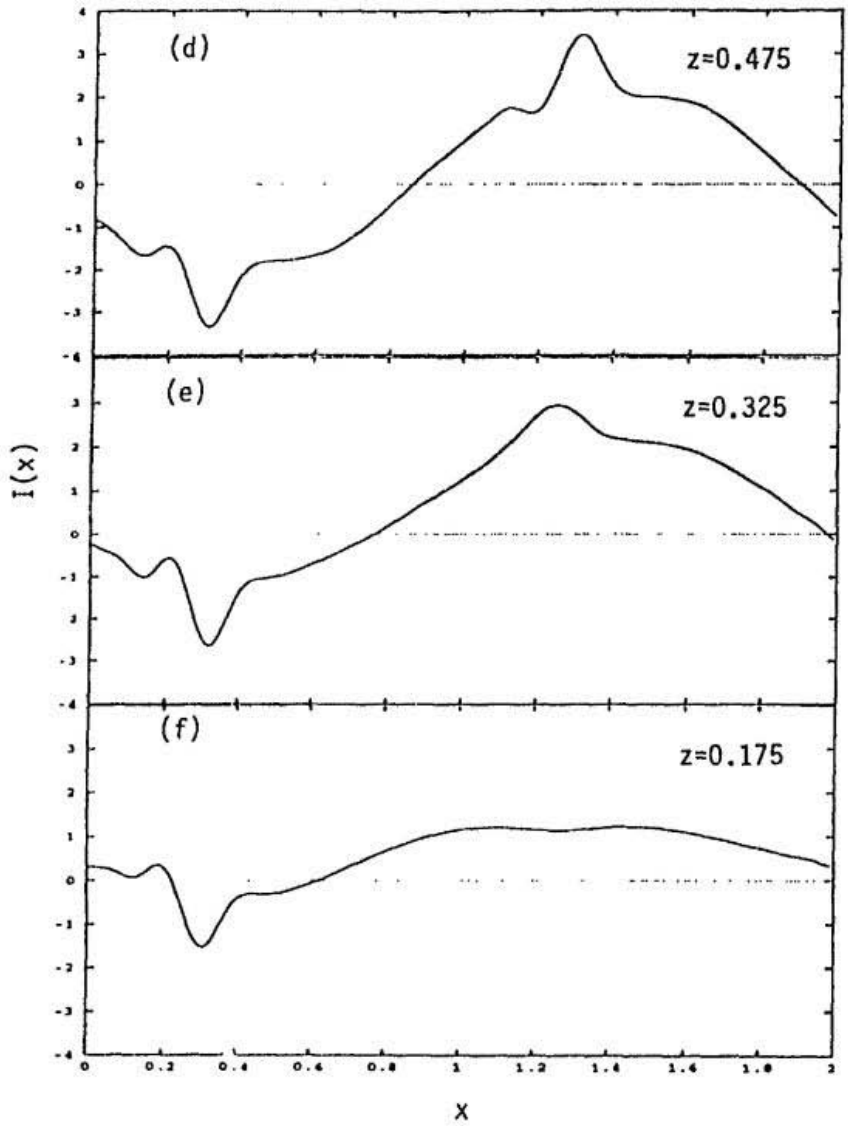

Figure 4.6: (continued).

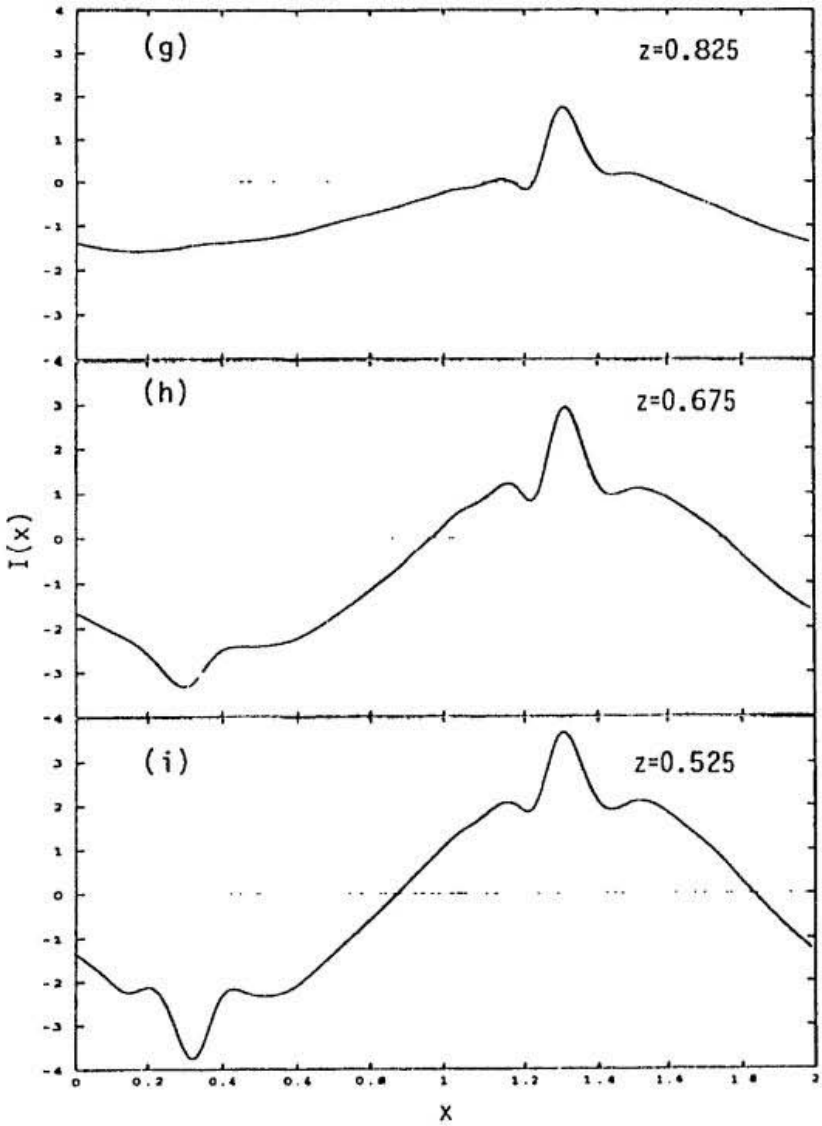

Figure 4.6: (continued).

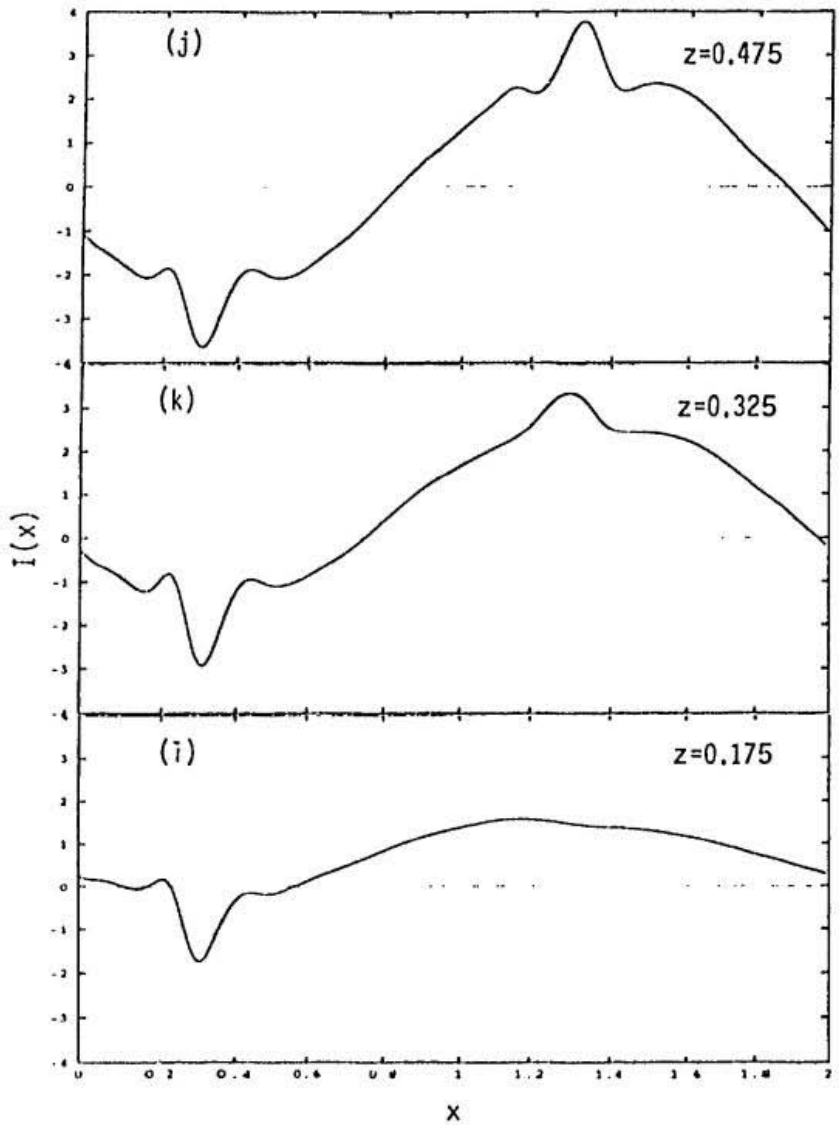

Figure 4.6: (continued).

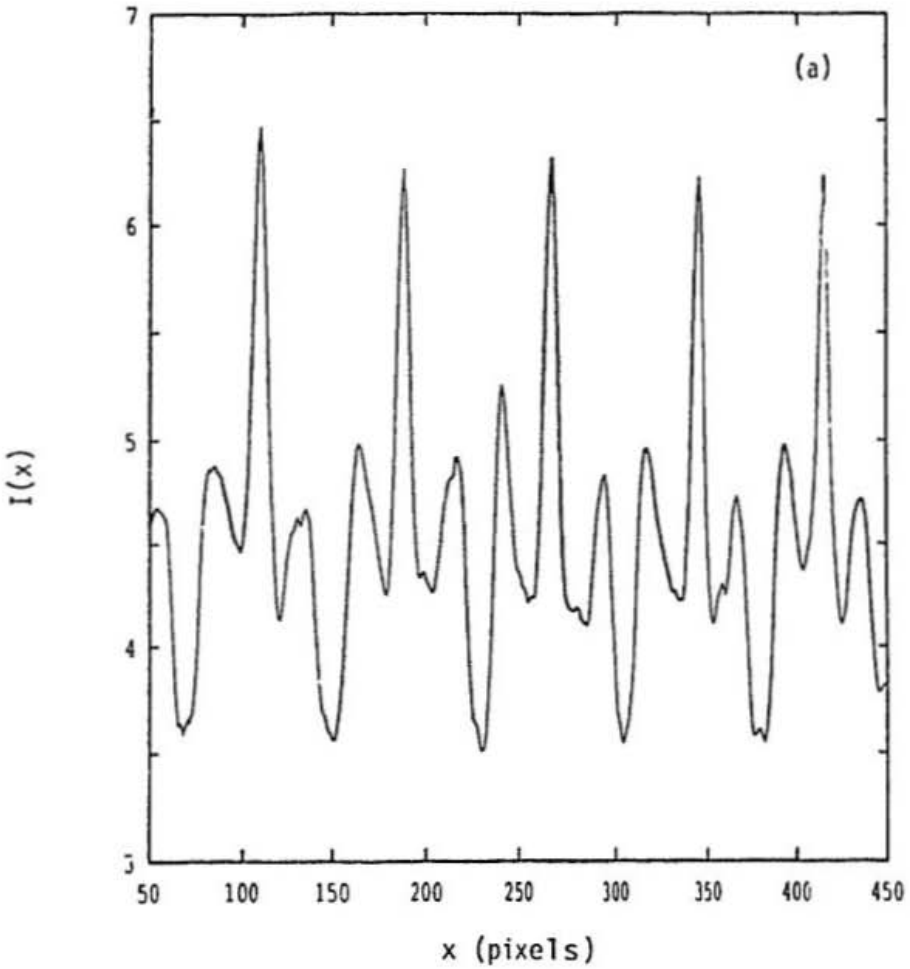

Figure 4.7: The experimental shadowgraph intensity, averaged over z, for (a) a SOC state of the mixture at $r = 1.54$ and (b) convection in pure water at $r = 1.19$. $I(x)$ is in arbitrary units and x in pixels.

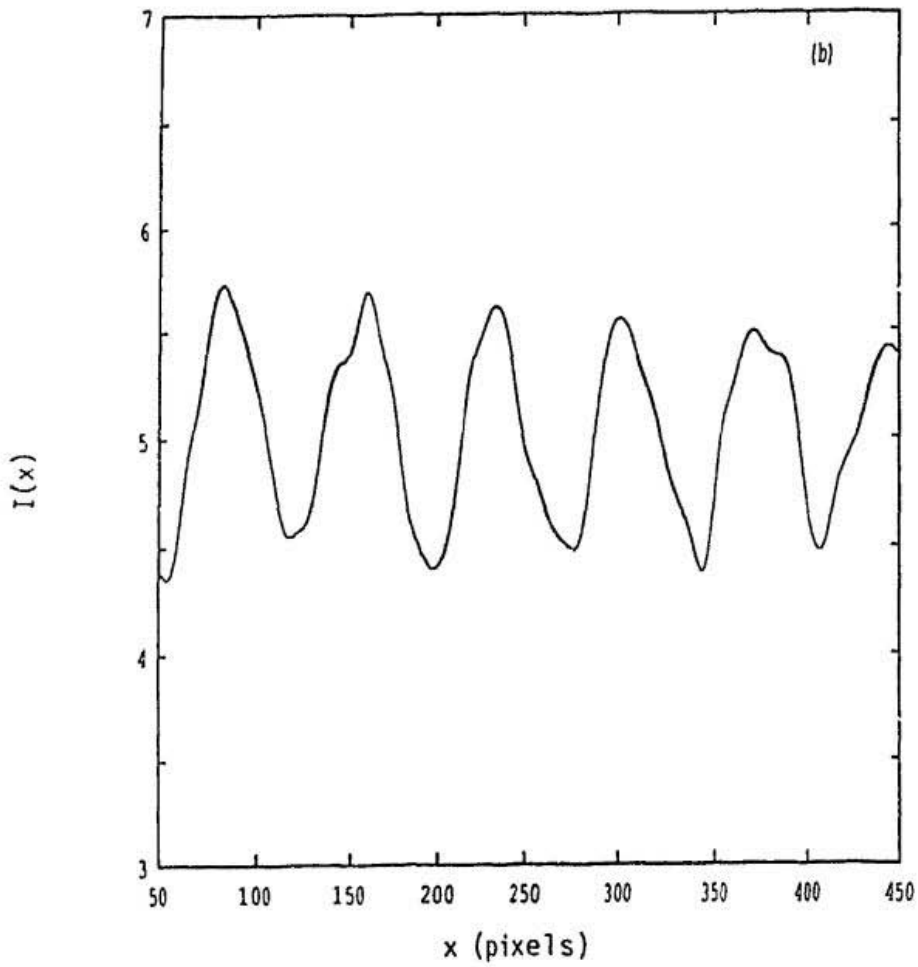

Figure 4.7: (continued).

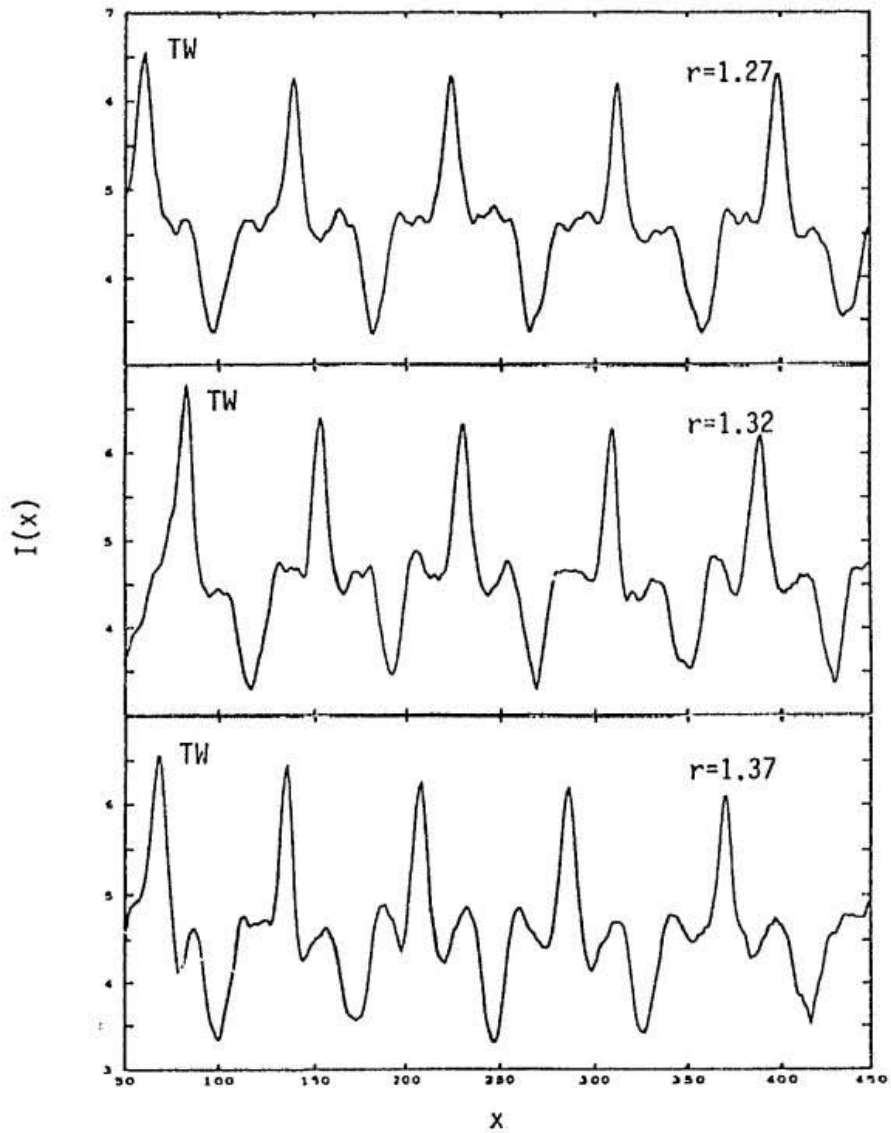

Figure 4.8: The experimental shadowgraph intensity, averaged over z, at various Rayleigh numbers. $I(x)$ is in arbitrary units and x in pixels.

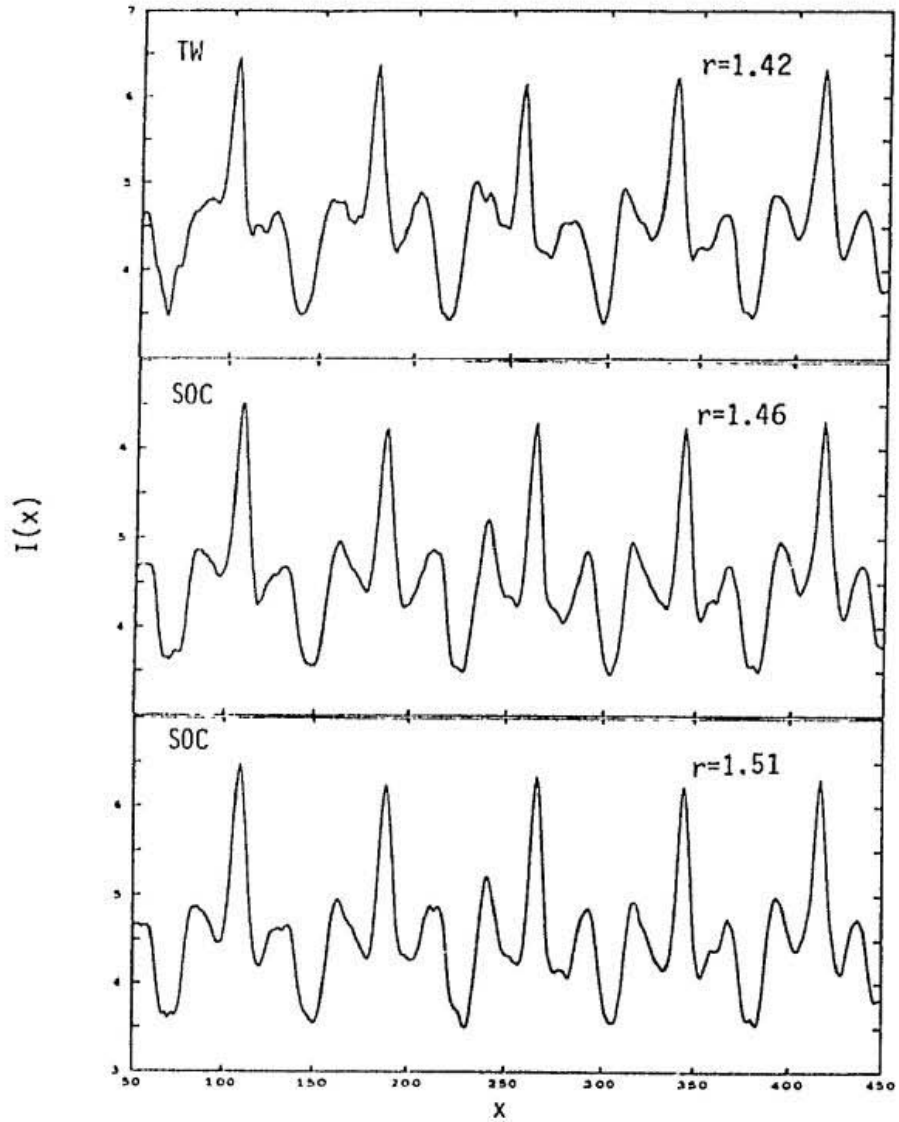

Figure 4.8: (continued).

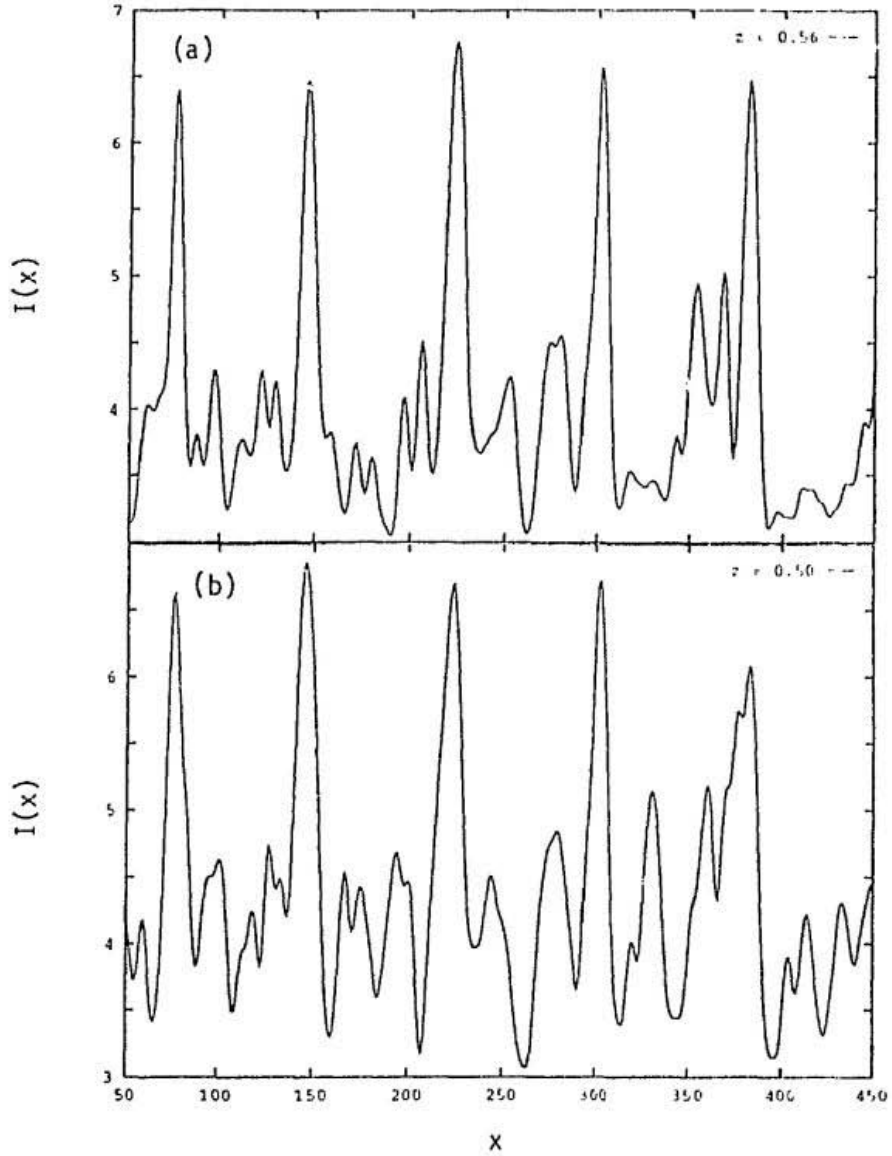

Figure 4.9: The experimental shadowgraph intensity for a TW state with $r = 1.29$ at various z positions. (a) $z = 0.56$, (b) $z = 0.50$, (c) $z = 0.44$ and (d) $z = 0.39$. $I(x)$ is in arbitrary units, z in units of d and x in pixels.

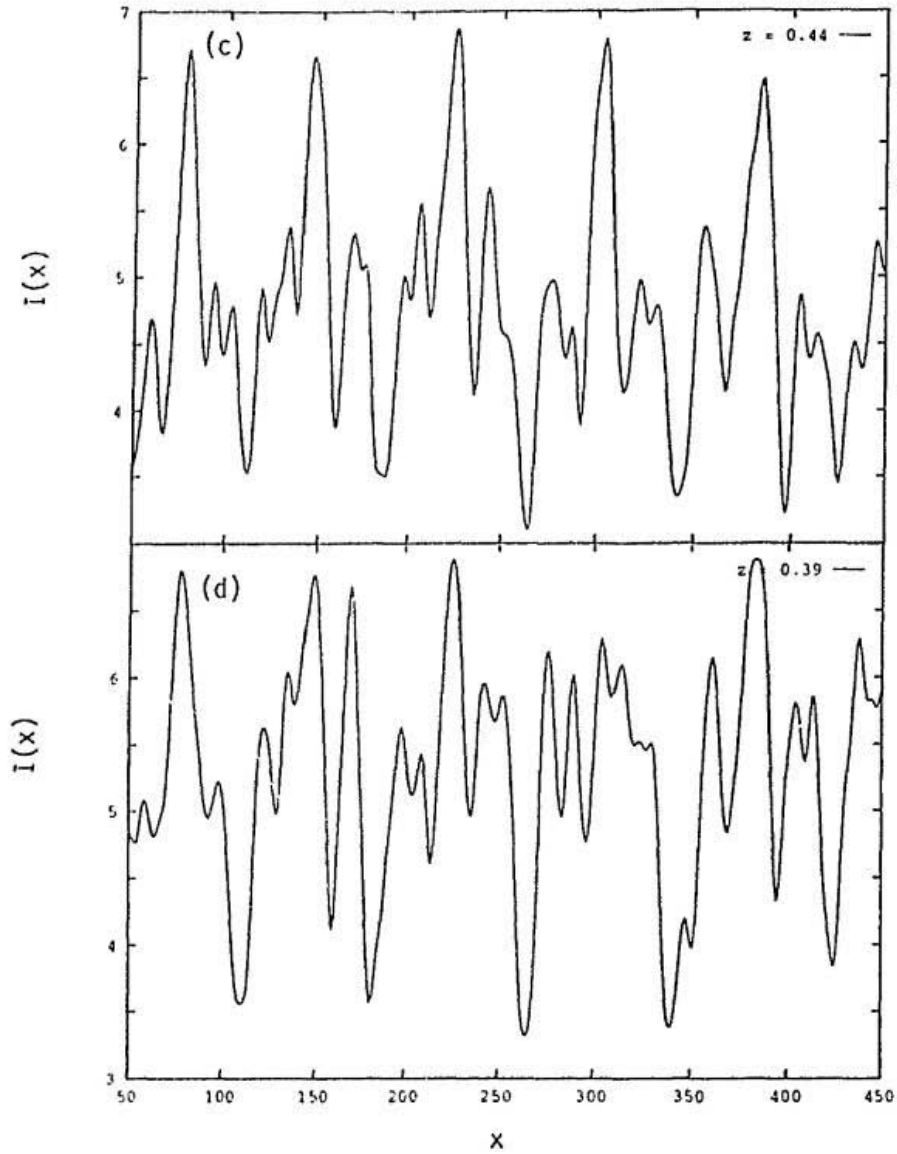

Figure 4.9: (continued).

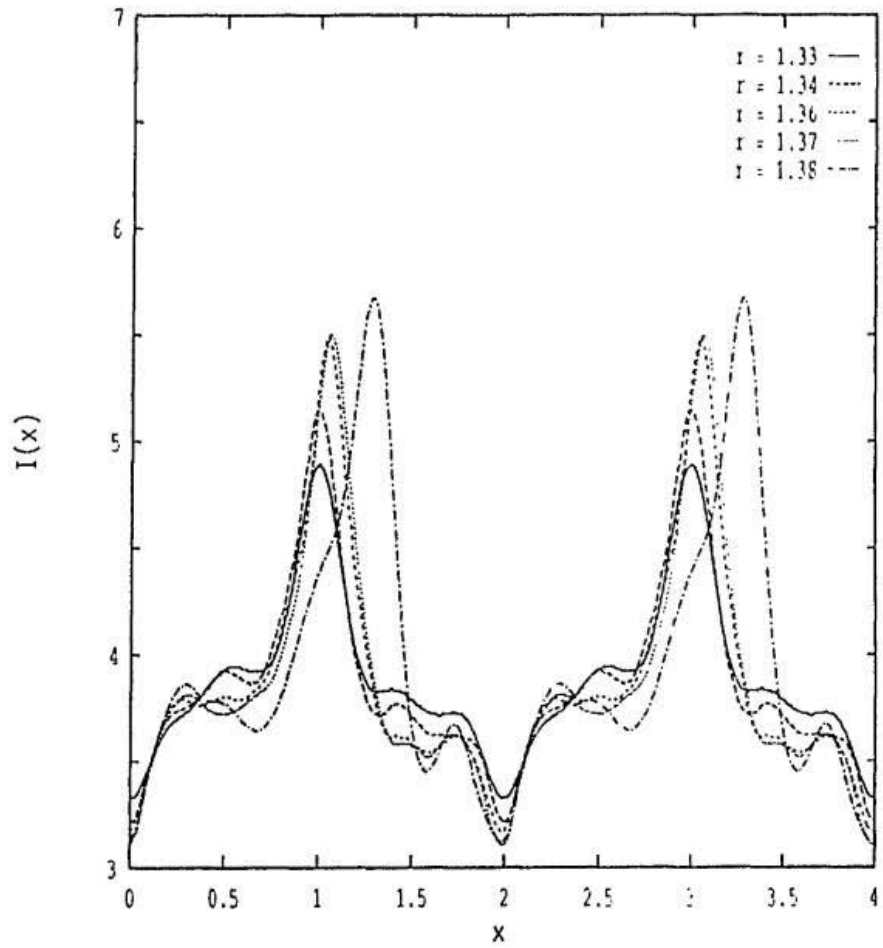

Figure 4.10: The experimental shadowgraph intensity profiles for TWs at various Rayleigh numbers, measured at a fixed point ($z = 0.5$) within the cell while the TWs passed by it. $I(x)$ is in arbitrary units and x in units of $a/2$.

Chapter 5

Conclusions

In this thesis, we presented the results of an experimental study of convection for an ethanol-water mixture in a quasi-one-dimensional cell. We studied the bifurcation properties of the mixture at the onset of convection and the evolution from TW states to SOC states. We found that at the onset of convection, the system undergoes a discontinuous transition from the conductive state to a TW state. The traveling wave frequency decreases as the Rayleigh number is increased, and eventually goes to zero at the transition from TW to SOC, in agreement with both theoretical and numerical predictions as well as other experimental observations. We also studied the role of the concentration field in the TW and SOC states by comparing our experimental shadowgraph intensity profiles with those predicted by numerical calculations. We confirmed the sharp features in the shadowgraph intensity, contributed mainly by the concentration field as predicted by numerical calculations. We were, however, unable to confirm the breaking of mirror symmetry in the TW states

predicted by the numerical results.

The comparison of our experimental results with the numerical ones is rather qualitative. This is in part due to the experimental difficulties encountered in this work. Noise and the limited resolution of our optical system prevented us from carrying out a good quantitative study of the shadowgraph intensity profiles and from calculating the concentration field from our data. Some of our results — for example, some qualitative differences between the measured and calculated intensity profiles (which were calculated for a laterally infinite system) and the difficulty we had in observing TW states in some runs — suggest that our quasi-one-dimensional geometry might have a significant effect on the dynamics of the convection. The numerical results of Barten *et al.* [13, 14] were calculated in the Boussinesq approximation, which assumes that the fluid properties are constant over the height of the fluid layer. In our experimental system, with $\Delta T_c \approx 9°C$, this approximation may be violated sufficiently that the dynamics are affected; in particular the viscosity of the mixture varies by about 30% across the cell at the convective onset (see Appendix A).

While this thesis was being written, we received an abstract and a preprint by Winkler and Kolodner [39, 40], who reported an experimental measurement of the concentration field in TW convection in ethanol-water mixtures. They conducted their experiment in a rectangular cell with an aspect ratio of $b : h = 3 : 1$ [40], which is ten times wider than ours and effectively two-dimensional. By using shadowgraph flow visualization from the side of the cell, they obtained very high quality shadowgraph intensity profiles. These intensity profiles were then integrated to produce a map of the two-dimensional refractive index field, which is further separated into two components due to

the convective temperature and concentration fields. Their results are in good agreement with the numerical predictions of Barten *et al.* [13].

It is obvious that a continuation of this work will require a substantial improvement in our optical system, to produce a less noisy shadowgraph intensity profile with higher resolution. Once this is done, further work suggested by our results can be taken on quantitatively. As mentioned above, the near one-dimensional geometry might play an important role in the dynamics of convection. Thus it would be of interest to continue to study the dynamical behaviour and the concentration field for TW and SOC states in this narrow geometry and compare our results with those done in a cell with bigger aspect ratio. More detailed measurements of the TW frequency near the transition from TW to SOC are also called for, to determine whether the transition is continuous in this narrow rectangular geometry.

Bibliography

[1] H. Bénard, *Rev. Gen. Sci. Pures Appl.* **11**, 1261 (1900); *Ann. Chim. Phys.* 23, 62 (1901).

[2] Rayleigh (Lord), *Philos. Mag.* **32**, 529 (1916).

[3] H. Stommel, A.B. Arons and D. Blanchard, *Deep Sea Res.* **3**, 152 (1956).

[4] D.T.J. Hurle and E. Jakeman, *J. Fluid Mech.* **47**, 667 (1971).

[5] G. Ahlers and I. Rehberg, *Phys. Rev. Lett.* **56**, 1373 (1986).

[6] I. Rehberg and G. Ahlers, *Phys. Rev. Lett.* **55**, 500 (1985); I. Rehberg and G. Ahlers, *Contemporary Mathematics* **56**, 277 (1986).

[7] E. Moses, J. Fineberg and V. Steinberg, *Phys. Rev. A* **35**, 2757 (1987); R. Heinrichs, G. Ahlers and D.S. Cannell, *ibid.* **35**, 2761 (1987).

[8] P. Kolodner, D. Bensimon and C.M. Surko, *Phys. Rev. Lett.* **60**, 1723 (1988); D. Bensimon, P. Kolodner, C.M. Surko, H.L. Williams and V. Croquette, *J. Fluid Mech.* **217**, 441 (1990).

[9] J.J. Niemela, G. Ahlers and D.S. Cannell, *Phys. Rev. Lett.* **64**, 1365 (1990); K.E. Anderson and R.P. Behringer, *Phys. Lett.* **A 145**, 323 (1990).

[10] P. Kolodner, *Phys. Rev. A* **42**, 2475 (1990).

[11] R.W. Walden, P. Kolodner, A. Passner and C.M. Surko, *Phys. Rev. Lett.* **55**, 496 (1985).

[12] D. Bensimon, A. Pumir and B.I. Shraiman, *J. Phys. (Paris)* **50**, 3089 (1989).

[13] W. Barten, M. Lücke and M. Kamps, in *Nonlinear Evolution of Spatiotemporal Structures in Dissipative Continuous Systems*, Edited by F.H. Busse and L. Kramer, Plenum Press (1990).

[14] W. Barten, M. Lücke, W. Hort and M. Kamps, *Phys. Rev. Lett.* **63**, 376 (1989).

[15] E. Moses and V. Steinberg, *Phys. Rev. A* **34**, 693 (1986).

[16] D. R. Ohlsen, S.Y. Yamamoto, C.M. Surko and P. Kolodner, *Phys. Rev. Lett.* **65**, 1431 (1990).

[17] K.D. Eaton, D.R. Ohlsen, S.Y. Yamamoto, C.M. Surko, W. Barten, M. Lücke, M. Kamps and P. Kolodner, *Phys. Rev. A* **43**, 7105 (1991).

[18] W. Barten and M. Lücke, private communication.

[19] S. Chandrasekhar, *Hydrodynamic and Hydromagnetic Stability*, Oxford University Press (1961).

[20] J.K. Bhattacharjee, *Convection and Chaos in Fluids*, World Scientific, 1987.

[21] J. Boussinesq, *Théorie analytique de la chaleur*, Vol. 2, Paris: Gauthier-Villars (1903).

[22] P.L. Silveston, *Forsch. Gebiete Ingenieurwes.* **24**, 29 and 59 (1958).

[23] H.T. Rossby, *J. Fluid Mech.* **36**, 309 (1969).

[24] K.E. Grew and T.L. Ibbs, *Thermal diffusion in gases*, Cambridge University Press (1952).

[25] H.J. Tyrrell, *Diffusion and Heat Flow in Liquids*, Butterworths, London (1961).

[26] B.J.A. Zielinska and H.R. Brand, *Phys. Rev. A* **35**, 1319 (1987).

[27] M.C. Cross and K. Kim, *Phys. Rev. A* **37**, 3909 (1988).

[28] H.R. Brand, P.C. Hohenberg and V. Steinberg, *Phys. Rev. A* **27**, 591 (1983); *Phys. Rev. A* **30**, 2548 (1984).

[29] B.J.A. Zielinska, D. Mukamel, V. Steinberg and S. Fishman, *Phys. Rev. A* **32**, 702 (1985).

[30] E. Knobloch, *Phys. Fluids* **23**, 1918 (1980).

[31] Minco Products, Inc., Bulletin HS-201.

[32] *Handbook of Chemistry and Physics*, edited by R.C. Weast, The Chemical Rubber Co., 1969.

[33] S. Rasenat, G. Hartung, B.L. Winkler and I. Rehberg, *Exp. in Fluids* **7**, 412 (1989).

[34] P. Kolodner and H. Williams, in *Nonlinear Evolution of Spatiotemporal Structures in Dissipative Continuous Systems*, Edited by F.H. Busse and L. Kramer, Plenum Press (1990).

[35] W. Merzkirch, *Flow Visualization*, Academic Press (1974).

[36] P. Kolodner, H. Williams and C. Moe, *J. Chem. Phys.* **88**, 6512 (1988).

[37] L. Catton, *Int. J. Heat Mass Transfer* **15**, 665 (1972).

[38] W.H. Press, B.P. Flannery, S.A. Teukolsky and W.T. Vetterling, *Numerical Recipes in C*, Cambridge University Press (1988).

[39] B.L. Winkler and P. Kolodner, *Bull. Amer. Phys. Soc.* **36**, 2689 (1991).

[40] B.L. Winkler and P. Kolodner, *J. Fluid Mech.*, to be published.

[41] *International Critical Tables*, edited by E. W. Washburn, McGraw-Hill, New York (1929).

[42] N.B. Vargaftik, *Tables on the Thermophysical properties of Liquids and Gases*, John Wiley & Sons (1975).

Appendix A

Some Properties of the Ethanol-Water Mixture

In this appendix, some relevant fluid properties of ethanol-water mixtures are given at different concentrations and temperatures. They are the heat capacity, the thermal conductivity λ, the density ρ and the viscosity μ. Values of these quantities corresponding to our experimental conditions are obtained from polynomial fits to the data in these tables. Data for the refractive index, Soret coefficient and mass diffusion coefficient are obtained from Table I of ref. [36].

c (wt %)	10°C	15°C	20°C	25°C	30°C	35°C	40°C
5.	0.99098	0.99032	0.98938	0.98817	0.98670	0.98501	0.98311
6.	0.98916	0.98877	0.98780	0.98656	0.98507	0.98335	0.98142
7.	0.98801	0.98729	0.98627	0.98500	0.98347	0.98172	0.97975
8.	0.98660	0.98584	0.98478	0.98346	0.98189	0.98009	0.97808
9.	0.98524	0.98412	0.98331	0.98193	0.98031	0.97846	0.97611
10.	0.98393	0.98301	0.98187	0.98013	0.97875	0.97685	0.97475
11.	0.98267	0.98171	0.98047	0.97897	0.97723	0.97527	0.97312
20.	0.97252	0.97068	0.96864	0.96639	0.96395	0.96134	0.95856
21.	0.97139	0.96914	0.96729	0.96495	0.96242	0.95973	0.95687
22.	0.97024	0.96818	0.96592	0.96348	0.96087	0.95809	0.95516
23.	0.96907	0.96689	0.96453	0.96199	0.95929	0.95643	0.95343
24.	0.96787	0.96558	0.96312	0.96048	0.95769	0.95476	0.95168
25.	0.96665	0.96424	0.96168	0.95895	0.95607	0.95306	0.94991
26.	0.96539	0.96287	0.96020	0.95738	0.95442	0.95133	0.94810
27.	0.96406	0.96144	0.95867	0.95576	0.95272	0.94955	0.94625
28.	0.96268	0.95996	0.95710	0.95410	0.95098	0.94774	0.94438
29.	0.96125	0.95844	0.95548	0.95241	0.94922	0.94590	0.94248
30.	0.95977	0.95686	0.95382	0.95067	0.94741	0.94403	0.94055

Table A.3: Density ρ (in g/cm^3) for ethanol-water mixtures at various concentrations (in weight percent) and temperatures (in °C). From [41].

c (Mole %)	3.0°C	23.0°C	41.0°C
0.0	4.211	4.182	4.174
2.02	4.316	4.236	4.241
4.16	4.379	4.271	1.291
6.16	4.395	4.312	4.320
8.91	4.362	4.324	4.324
11.5	4.282	4.299	4.299
14.4	4.186	4.241	4.257
20.7	3.925	4.077	4.107
28.1	3.622	3.847	3.898
37.0	3.367	3.588	3.655
47.7	3.132	3.329	3.401
61.0	2.802	3.010	3.132
77.9	2.568	2.760	2.861
100.0	2.263	2.417	2.601

Table A.1: Heat capacity (in J/gK) for ethanol-water mixtures at various concentrations c (in Mole percent) and temperatures (in °C). From [41].

c (wt %)	0.0°C	20.0°C	40.0°C	60.0°C	80.0°C
0	0.565	0.599	0.628	0.652	0.670
20	0.451	0.471	0.490	0.505	0.516
40	0.352	0.364	0.373	0.381	0.386
60	0.273	0.276	0.279	0.283	0.285
80	0.213	0.212	0.209	0.208	0.206
100	0.172	0.167	0.162	0.157	0.152

Table A.2: Thermal conductivity λ (in W/mK) for ethanol-water mixtures at various concentrations (in weight percent) and temperatures (in °C). From [42].

c (wt. %)	0°C	10°C	20°C	25°C	30°C	40°C	50°C	60°C	70°C
10	32.15	21.62	15.48	13.28	11.53	8.96	7.25	6.02	5.09
20	52.75	32.35	21.68	18.08	15.39	11.44	8.96	7.28	6.06
30	69.0	40.95	26.70	22.03	18.49	13.53	10.38	8.26	6.77
40	71.5	43.55	28.67	23.74	19.91	14.55	11.16	8.87	7.24
45	70.1	43.1	28.67	23.87	20.07	14.78	11.38	9.02	7.36
50	66.25	41.74	28.32	23.68	20.01	14.75	11.36	9.04	7.39
60	57.15	37.87	26.12	22.32	19.06	14.26	11.09	8.87	7.27
70	47.2	32.68	23.69	20.25	17.44	13.28	10.44	8.41	6.96
80	36.48	26.63	19.98	17.38	15.19	11.81	9.50	7.78	6.48
90	26.94	20.48	16.01	14.22	12.70	10.22	8.35	6.95	5.89
100	17.76	14.80	12.21	11.01	9.97	8.24	6.95	5.90	5.06

Table A.4: Viscosity μ (in 0.001 g/cms) for ethanol-water mixtures at various concentrations (in weight percent) and temperatures (in °C). From [41].